

AD-A073 701

OREGON GRADUATE CENTER BEAVERTON  
FIELD ELECTRON AND ION SOURCE RESEARCH FOR HIGH DENSITY INFORMAT--ETC(U)  
AUG 77 L W SWANSON

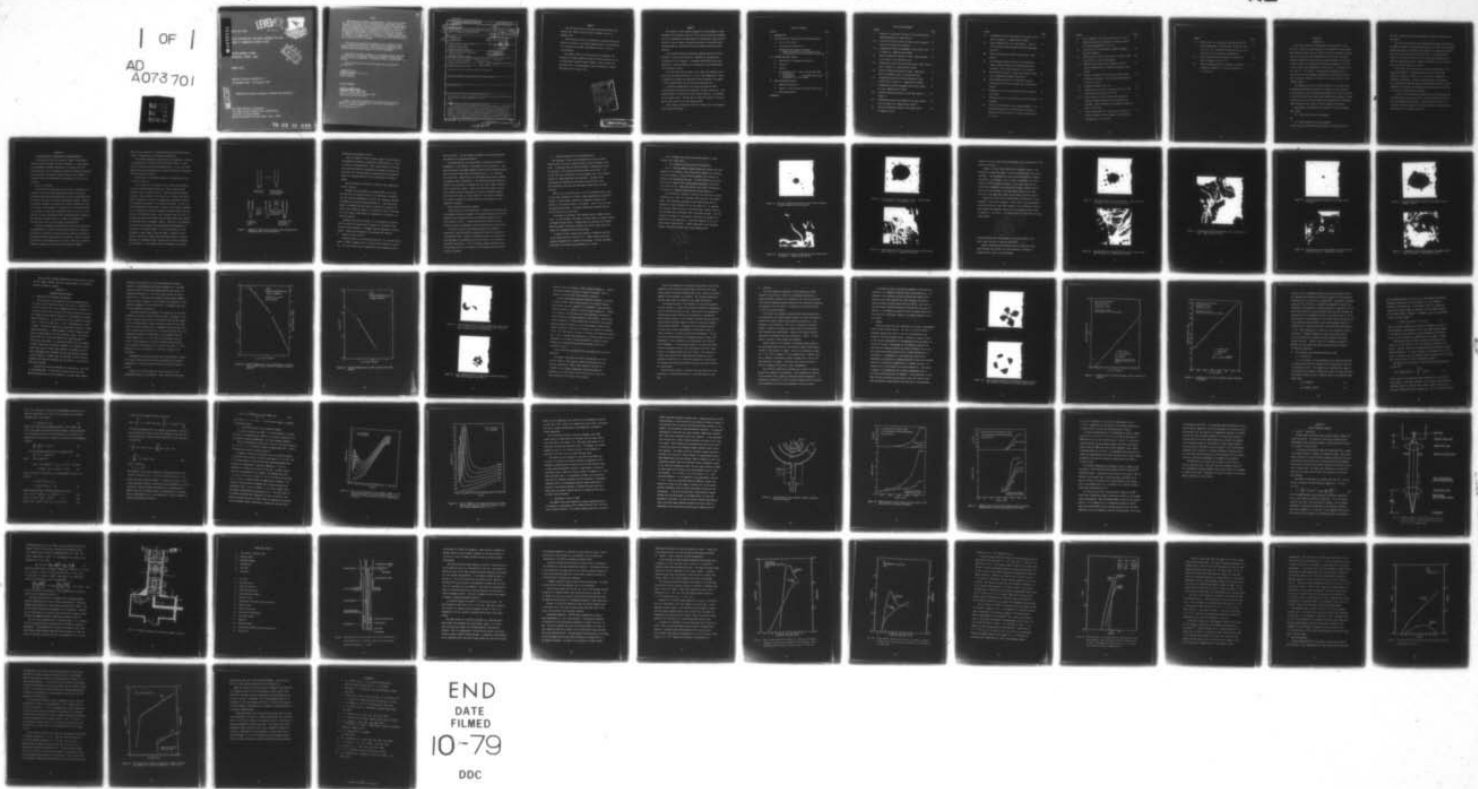
F/G 20/3  
F33615-76-C-1327

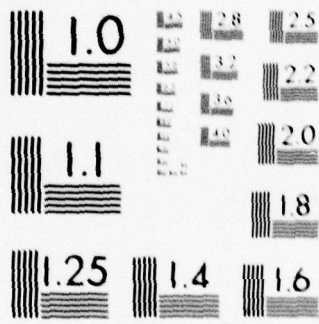
UNCLASSIFIED

AFAL-TR-77-160

NL

| OF |  
AD  
A073 701





MICROCOPY RESOLUTION TEST CHART

AD A 073701

LEVEL II (2)

A072541



AFAL-TR-77-160

FIELD ELECTRON AND ION SOURCE RESEARCH FOR HIGH DENSITY INFORMATION STORAGE SYSTEM

OREGON GRADUATE CENTER  
BEAVERTON, OREGON 97005



AUGUST 1977

INTERIM TECHNICAL REPORT No. 3  
15 NOVEMBER 1976 - 15 FEBRUARY 1977

APPROVED FOR PUBLIC RELEASE; DISTRIBUTION UNLIMITED.

DDC FILE COPY

AIR FORCE AVIONICS LABORATORY  
AIR FORCE WRIGHT AERONAUTICAL LABORATORIES  
AIR FORCE SYSTEMS COMMAND  
WRIGHT-PATTERSON AIR FORCE BASE, OHIO 45433

79 09 10 072

NOTICE

When Government drawings, specifications, or other data are used for any purpose other than in connection with a definitely related Government procurement operation, the United States Government thereby incurs no responsibility nor any obligation whatsoever; and the fact that the government may have formulated, furnished, or in any way supplied the said drawings, specifications, or other data, is not to be regarded by implication or otherwise as in any manner licensing the holder or any other person or corporation, or conveying any rights or permission to manufacture, use, or sell any patented invention that may in any way be related thereto.

The views and conclusions contained in this document are those of the authors and should not be interpreted as necessarily representing the official policies, either expressed or implied, of the Advanced Research Projects Agency or the U.S. Government.

This report has been reviewed by the Information Office (OI) and is releasable to the National Technical Information Service (NTIS). At NTIS, it will be available to the general public, including foreign nations.

This technical report has been reviewed and is approved for publication.

*Millard G. Mier*

---

MILLARD G. MIER  
Project Engineer

FOR THE COMMANDER

*Robert J. Almassy*

---

ROBERT J. ALMASSY, Maj, USAF  
Acting Chief, Electronic Research Branch  
Electronic Technology Division

Copies of this report should not be returned unless return is required by security considerations, contractual obligations, or notice on a specific document.

Unclassified

SECURITY CLASSIFICATION OF THIS PAGE (When Data Entered)

19 REPORT DOCUMENTATION PAGE		READ INSTRUCTIONS BEFORE COMPLETING FORM
1. REPORT NUMBER 18 AFAL-TR-77-169	2. GOVT ACCESSION NO.	3. RECIPIENT'S CATALOG NUMBER 9
4. TITLE (and Subtitle) 6 FIELD ELECTRON AND ION SOURCE RESEARCH FOR HIGH DENSITY INFORMATION STORAGE SYSTEM		5. TYPE OF REPORT & PERIOD COVERED Interim Technical Report, No. 3, 15 Nov 77-15 Feb 1977
7. AUTHOR(s) 10 L. W. Swanson		8. PERFORMING ORG. REPORT NUMBER 1
9. PERFORMING ORGANIZATION NAME AND ADDRESS Oregon Graduate Center 19600 N.W. Walker Road Beaverton, Oregon 97005		10. PROGRAM ELEMENT, PROJECT, TASK AREA & WORK UNIT NUMBERS 16 17 Project 3164-01-01
11. CONTROLLING OFFICE NAME AND ADDRESS Advanced Research Projects Agency 1400 Wilson Blvd. Arlington, Virginia 22209		12. REPORT DATE 11 August 1977
14. MONITORING AGENCY NAME & ADDRESS (if different from Controlling Office) Air Force Avionics Laboratory (DHR) Air Force Systems Command Wright-Patterson AFB, Ohio 45433 1272p.		13. NUMBER OF PAGES 62
		15. SECURITY CLASS. (of this report) Unclassified
16. DISTRIBUTION STATEMENT (of this Report)  Approved for public release, distribution unlimited		15a. DECLASSIFICATION/DOWNGRADING SCHEDULE
17. DISTRIBUTION STATEMENT (of the abstract entered in Block 20, if different from Report)		
18. SUPPLEMENTARY NOTES		
19. KEY WORDS (Continue on reverse side if necessary and identify by block number)  Field emission, field ion emission, field electron emission, high brightness electron source, high brightness ion source		
20. ABSTRACT (Continue on reverse side if necessary and identify by block number)  The purpose of this research program is the development of high brightness field emission and field ion sources. A new method of preparing W/Zr TF cathodes is discussed and life test results of LaB <sub>6</sub> field emitters are described. Built up emitters of tantalum and iridium have been examined. Results of experiment and calculation are presented for the energy distribution of field emitted electrons from substrates of varying temperature and work function. Field ionization data for several gases has been obtained. Also, noise measurements have been performed for a field ion source.		

DD FORM 1 JAN 73 1473 EDITION OF 1 NOV 65 IS OBSOLETE

Unclassified

SECURITY CLASSIFICATION OF THIS PAGE (When Data Entered)

390077

4/B

PREFACE

This technical report covers the research performed under Contract No. F33615-76-C-1327 from 15 November 1976 to 15 February 1977.

This contract is with the Department of Applied Physics and Electronic Science of the Oregon Graduate Center, with Professor L. W. Swanson as principal investigator and Dr. A. Bell as co-investigator.

The primary thrust of the work was the development and evaluation of high brightness electron and wire sources for use in high density archival memory systems. Work was under the direction of Mr. John Blasingame, Avionics Laboratory, Wright-Patterson Air Force Base, Ohio.

Accession For	
NTIS GAMA I	<input checked="" type="checkbox"/>
DIC TAB	<input type="checkbox"/>
Unannounced	<input type="checkbox"/>
Justification	
By	
Distribution/	
Availability Codes	
Dist	Avail and/or special
A	

PREVIOUS PAGE BLANK

## SUMMARY

The purpose of this research program is the development of high brightness field emission sources of both ions and electrons suitable for use in information storage systems. In particular, field electron sources of various types of materials and modes of operation along with gas phase and liquid film field ionization sources are being examined.

A new method of making zirconiated tungsten emitters has been developed using an electrophoretic technique for deposition of zirconium on to the tungsten. A tantalum carbide emitter was also fabricated. Work has begun on the preparation of zone melted  $\text{LaB}_6$  field emission crystals.

Life tests have been carried out for  $\text{LaB}_6$  field emitters one of which has been operated briefly at 1 mA at room temperature. Built-up emitters of iridium and tantalum have been examined; both appear to offer possibilities for practical field emission use.

A detailed examination of the energy distribution (TED) characteristics of  $\text{LaB}_6$  and Zr/W emitters has been carried out. The energy spread of the built-up W(100) cathode appears to be dependent on the aperture size. The TED work is important because it directly affects spot size of the field emission beam.

Xenon, argon and hydrogen field ion currents have been examined under various conditions.

## TABLE OF CONTENTS

SECTION	PAGE
I. INTRODUCTION	1
II. EMITTER MATERIALS FABRICATION AND CHARACTERIZATION	3
A. The Zr/W TF Cathode	3
B. Tantalum Carbide Emitters	6
C. Hexaboride Field Emission Cathodes	7
1. Sample Preparation for Electronmicroscopy	8
2. Micrographs and Electron Diffraction Patterns	9
III. ELECTRON EMISSION STUDIES	17
A. Hexaborides of Lanthanum and Samarium	17
B. Tantalum	24
C. Iridium	25
D. Field Emission Total Energy Distribution (TED)	29
1. Introduction	29
2. Calculated Values of Full Width Half Maxima	33
3. Experimental Values of FWHM	36
IV. FIELD IONIZATION STUDIES	43
A. Apparatus Description	43
B. Results - Field Ionization Current/Voltage Data	51
C. Noise Measurements	57
REFERENCES	62

## LIST OF ILLUSTRATIONS

FIGURE		PAGE
1.	Sequence of operations involved in electrophoretically depositing $ZrH_2$ on a field emitter.	5
2a.	Electron diffraction pattern of $LaB_6$ crystal prepared by molten aluminum flux technique.	10
2b.	Transmission electron micrograph of $LaB_6$ crystal used in Figure 2a. Magnification 48,000.	10
3a.	Electron diffraction pattern of $LaB_6$ . Same specimen as in Figure 2, but different area.	11
3b.	Transmission electron microscope pattern of $LaB_6$ crystal used in Figure 3a. Magnification 50,000.	11
4a.	Electron diffraction pattern of $LaB_6$ . Same specimen as in Figures 2 and 3 but different area.	13
4b.	Transmission electron microscope pattern of $LaB_6$ crystal used in Figure 4a. Magnification 48,000.	13
5.	Transmission electron micrograph from a new crystal of $LaB_6$ . Magnification 30,000.	14
6a.	Electron diffraction pattern of the $LaB_6$ crystal of Figure 5.	15
6b.	Transmission electron micrograph of the $LaB_6$ crystal used for Figure 6a. Magnification 42,000.	15
7a.	Electron diffraction pattern of the $LaB_6$ crystal of Figures 5 and 6.	16

FIGURE	PAGE
7b. Transmission electron micrograph of the $\text{LaB}_6$ crystal used for Figure 7a. Magnification 37,000.	16
8a. Fowler Nordheim plot for a $\text{LaB}_6$ emitter. Inset is for the probe current through a 0.08 milliradian aperture.	19
8b. Fowler Nordheim plot of probe current from a $\text{LaB}_6$ emitter.	20
9a. Field emission pattern of $\text{LaB}_6$ emitter made $\text{LaB}_6$ single crystals grown by the aluminum molten flux technique. Note irregular nature of the pattern.	21
9b. Field emission pattern of $\text{LaB}_6$ after repeated flashing at temperatures greater than $2000^\circ\text{K}$ .	21
10. Field emission patterns of a thermally annealed (Figure 10a) and built-up (Figure 10b) iridium field emitter.	26
11. Arrhenius plot for field assisted surface diffusion of iridium.	27
12. Arrhenius plot for field assisted surface diffusion of tungsten.	28
13. Plot of the full-width at half maximum (FWHM) for the energy distribution of field emitted electrons as a function of electron field $F$ at various temperatures; $\phi = 2.5 \text{ V}$ .	34

FIGURE	PAGE
14. Plot of FWHM for the energy distribution of field emitted electrons as a function of electric field $F$ at various temperatures; $\phi = 4.5$ V.	35
15. Cross section of the concentric sphere retarding potential analyzer.	38
16. FWHM and probe current versus electric field at $78^\circ\text{K}$ and $1675^\circ\text{K}$ for zirconiated tungsten.	39
17. FWHM and probe current versus electric field at various temperatures for a built-up tungsten field emitter.	40
18. Schematic diagram of the SIM optical system (beam deflectors not shown). Only one deflection system is used at a time.	44
19. Schematic diagram of the SIM.	46
20. Drawing of the FI source. Aperture size is 0.5 mm, emitter-aperture spacing 0.5-1.5 mm.	48
21. Probe current and total current as a function of emitter voltage as measured in the SIM near the specimen. Angle subtended by the objective aperture was $\alpha = 0.012$ rad.	52
22. Probe current and total current as a function of emitter voltage for Ar as measured in the SIM near the specimen, $\alpha = 0.012$ rad.	53

FIGURE	PAGE
23. Total current vs. voltage with the same emitter for H <sub>2</sub> and argon gases. Note the shift in the I-V curve for Ar at 77 K. Ionization potentials are I <sub>p</sub> = 15.7 eV and 15.6 eV for Ar and H <sub>2</sub> , respectively.	55
24. Total current and probe current as a function of emitter voltage for Xe at 77 K.	58
25. Total and probe current as a function of emitter voltage for methane at 77 K and a pressure of $2 \times 10^{-3}$ torr.	60

## SECTION I

### INTRODUCTION

This report describes progress made during the third 3 month period on a research program aimed at the development of high brightness charged particle sources suitable for use in information storage systems. In particular the charged particle source and focussing system envisioned for this application must be capable of providing a particle beam with sufficient flux density and smallness of size to write and/or read information at less than 0.1  $\mu\text{m}$  resolution and at a rate of  $\sim 10^7$  bits/sec. Because such requirements place a severe limit on the brightness requirements of the particle source, very few sources remain in contention as a viable option for such a memory system.

The primary aim of this research program is to evaluate high brightness field emission sources with respect to their potential for satisfying the above mentioned requirements for a particle source. In view of the fact that present high density archival memory schemes include both ion and electron beams this research will be examining field ionization (FI) as well as field electron (FE) sources.

Specifically this research is divided into the two following major tasks:

(1) Field Electron Source Development

and

(2) Field Ionization Source Development

In each task new source materials and modes of operation will be

developed coupled with detailed evaluation of emission characteristic properties.

The field electron source work described here deals with built-up cathodes of tungsten, iridium and tantalum; so far the built-up tungsten cathode operated in the thermal field emission (TF) mode has proved to be a practical and long lived electron source. Its energy spread appears to be greater than that of the zirconiated tungsten source when wide apertures are used. Whether this holds true for the other built-up cathodes remains to be seen.

Further work has been carried out with the hexaborides of lanthanum and samarium. A lanthanum hexaboride emitter has been operated at emission currents up to 1 mA at room temperature - a remarkable performance. Because of the difficulty of obtaining well ordered field emission spatial distributions with  $\text{LaB}_6$  crystals prepared by the molten flux technique, future work will be directed to the use of zone-melted  $\text{LaB}_6$  crystals.

A careful energy distribution (TED) study both experiments and calculations has been carried out for both the zirconiated and the built-up tungsten field emitters. The motivation for this is the fact that the energy spread of the electron source is frequently the limiting factor in reducing spot size.

## SECTION II

### EMITTER MATERIALS FABRICATION AND CHARACTERIZATION

As discussed in the first quarterly report, field emitter materials may be divided into three categories: 1) pure metals, 2) heterogeneous cathodes consisting of a surface layer on a solid substrate, and 3) homogeneous metalloid compounds and alloys. The zirconiated 100 oriented tungsten emitter is an example of category 2 while the hexaborides and carbides fall into the latter group.

#### A. The Zr/W TF Cathode

The Zr/W emitter operating in the TF mode is proving to be a reliable, long lived, high brightness electron source having favorable energy spread characteristics as will be discussed later in the work covering total energy distribution studies. Because the present technique of applying the zirconium component by hand in the form of  $ZrH_2$  powder to the upper part of the emitter shank is a delicate one requiring considerable skill on the part of the operator, we have investigated other possible methods of applying the zirconium coatings in order to reduce the dependence on critical skills and to ensure greater reproducibility.

An earlier technique of applying the zirconium by evaporation was abandoned due to difficulty in applying sufficient zirconium and because this method of application also deposits zirconium on the hairpin filament which supports the emitter. When the emitter is operated at high temperatures (TF mode of operation), unwanted thermionic emission then occurs from the hairpin filament.

Hence any new technique for applying zirconium preferably should result in depositing it on the emitter shank only.

Two possible methods for doing this were considered: alloying the zirconium with tungsten before preparing emitters or applying the zirconium as  $ZrH_2$  electrophoretically. So far, the latter method has been investigated and a workable procedure for applying the  $ZrH_2$  has been developed.

The sequence of operations employed for depositing the  $ZrH_2$  is shown in Figure 1.

A 5 mil blank of 100 oriented W wire is first spot welded to a hairpin supporting and heating loop. Next a regular field emission point is etched by the d.c. drop-off method in 2N NaOH solution. The next step is the critical one in which the electrophoretic deposition of  $ZrH_2$  is accomplished by making the emitter 45 V negative with respect to a platinum electrode. In the technique developed for this project, a slurry of  $ZrH_2$  powder suspended in a 2:1 mixture (by volume) of methanol and amyl acetate was used as the electrophoresis liquid. About 100 mg of  $ZrH_2$  per 20 ml of solution was used and the powder was thoroughly mixed and dispersed by agitating with an ultrasonic cleaner. When this was completed, the emitter and electrode were inserted and electrophoresis was carried out for 30-100 seconds. In an earlier variant of this technique, a small amount of HCl was added to increase conductivity of the slurry; however the conditions required to deposit the  $ZrH_2$  in a reasonably short time also led to severe corrosion of the emitter. In the present HCl free technique, the current

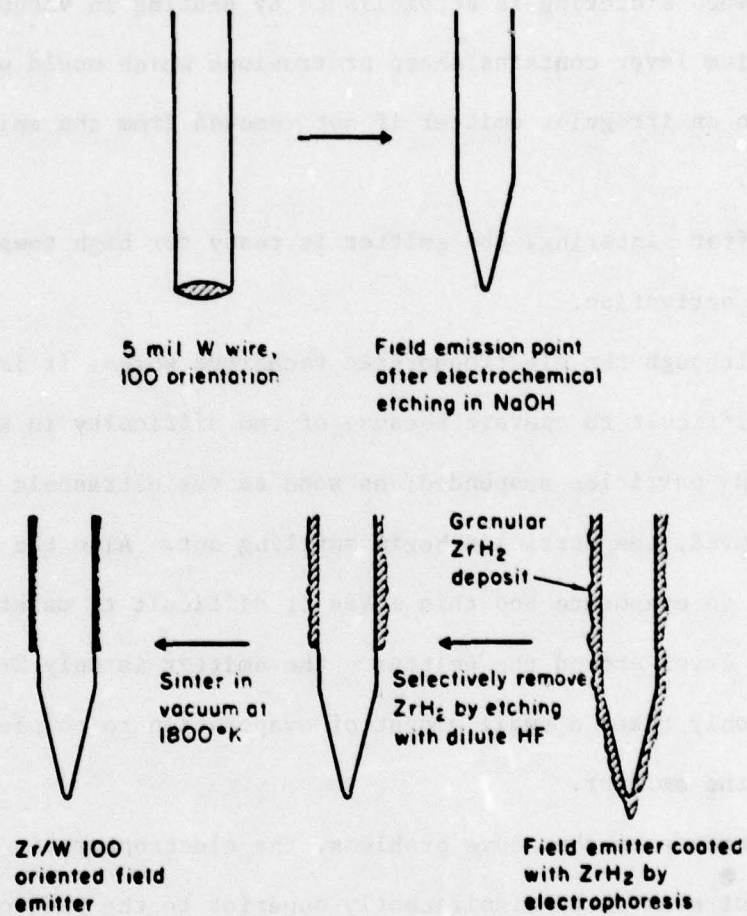


**Figure 1. Sequence of operations involved in electrophoretically depositing ZrH<sub>2</sub> on a field emitter.**

flowing was approximately 100  $\mu$ A.

When the deposit of  $ZrH_2$  is thick enough, the  $ZrH_2$  directly surrounding the emitter is removed by etching briefly (< 1 sec) in dilute or concentrated HF. This is done because in the next step, when sintering is accomplished by heating in vacuum, the zirconium layer contains sharp protrusions which would possibly lead to an irregular emitter if not removed from the emitter region.

After sintering, the emitter is ready for high temperature vacuum activation.

Although the electrophoretic technique works, it is somewhat difficult to operate because of the difficulty in keeping the  $ZrH_2$  particles suspended: as soon as the ultrasonic agitation is removed, the particles begin settling out. Also the solvent begins to evaporate and this makes it difficult to maintain the slurry level around the emitter - the emitter is only 2-3 mm long, so it only takes a small amount of evaporation to completely uncover the emitter.

Because of the above problems, the electrophoretic approach does not seem to be significantly superior to the previous deposition by hand technique. We suggest that the remaining, alloying, approach should be investigated for preparing W/Zr emitters.

#### B. Tantalum Carbide Emitters

Tantalum carbide is an interesting material; its extreme melting point ( $\sim 4000^\circ\text{C}$ ) suggests that it would be very resistant to vacuum arc. For this reason we have regarded TaC as a potentially useful

emitter material. In this report we discuss our initial experience with emitters of carburized tantalum.

A tantalum emitter was etched using<sup>1</sup> a solution of 48% HF(2) + CH<sub>3</sub>COOH(0.5) + conc H<sub>3</sub>PO<sub>4</sub>(1) + 36N H<sub>2</sub>SO<sub>4</sub>(1) at 5-10 volts d.c. The resulting emitter was judged adequate from its field emission pattern. Next the tip was carburized with benzonitrile at ~ 5 μ pressure for 60 seconds. Unfortunately the resulting surface did not exhibit any symmetry after carburization. The resulting carbide surface is probably very resistant to diffusion so that local surface excesses will not smooth out easily. Future work with this emitter will involve careful in-situ carburization in order to carefully monitor and control the extent of carbon addition. The in-situ technique will involve heating the tantalum emitter in the presence of low pressures of methane.

#### C. Hexaboride Field Emission Cathodes

Field emitters of the hexaborides of lanthanum and samarium have been examined under this program. The crystal blanks used have been prepared by the aluminum molten flux technique discussed in the first quarterly report. A characterization of them by electron diffraction and by transmission electron microscopy is given below:

The defect structure and possible impurity of lanthanum hexaboride is being studied by transmission electron microscopy on a Hitachi HU 11-B-3. Effective thinning processes, to prepare the LaB<sub>6</sub> specimens for examination in the microscope, are also being developed concurrently. In the following, sample preparation will be discussed firstly, with examples of micrographs and diffraction patterns following.

## 1. Sample Preparation for Electronmicroscopy

The specimens of  $\text{LaB}_6$  under investigation are thin crystal platelets with the broad surfaces having an area of between 1- and 2  $\text{mm}^2$ . A Fischione twin-jet electropolisher is being used to thin the crystals. Two solutions have been tested in the unit: a 6 percent solution of perchloric acid in methanol, and a 2.25 percent solution of sodium hypochlorite in methanol. Because of the difficulties of handling the perchloric acid solution in the electropolisher, more time has been spent working with the other solution.

Given a particular solution to use in the Fischione unit, there are two other parameters to control, namely temperature and applied voltage. In most cases, lowering the temperature improves the quality of the thinned region of the sample. This is true for  $\text{LaB}_6$  and sodium hypochlorite. The lowest temperature obtained thus far was 8°C using an ice water bath.

As voltage is increased, three general types of sample erosion occur. At low voltages, the sample is etched, while at higher voltages the sample becomes pitted. Between these two extremes lie voltages where the sample is properly thinned, with fairly large areas thin enough for transmission electron microscopy.

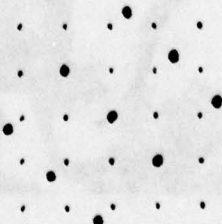
A series of four voltages were applied to different crystals, in the range from one to ten volts d.c. These crystals were subsequently examined with a Siemens metallograph. The best specimens were found to be those electropolished at 6.5 volts.

After thinning, the crystals have been mounted on copper washers with silver paint.

## 2. Micrographs and Electron Diffraction Patterns

As yet, only the samples prepared using low voltages have been examined in the Hitachi. Very few suitable regions were available in these crystals. In the following examples, the technique of selected area diffraction was used. For each diffraction pattern, only the area shown in the corresponding micrograph contributed to the spots in it. These patterns are still under investigation, but there are a couple of features that can be pointed out.

In the first pair (Figures 2a and 2b), the diffraction pattern is made up of at least two superposed [100] patterns, and probably three. The micrograph, although of poor quality does show the presence of a grain boundary on the left hand side. By changing the projector lens pole piece in the microscope, Figures 3a and 3b were obtained from a different area of the same specimen. Note the presence of streaks in this pattern, indicating the presence of a precipitate in the  $\text{LaB}_6$  matrix. There also appears to be a different type of pattern (non - [100]) superposed on the  $\text{LaB}_6$ [100] pattern, indicated in heavy dots in the diagram below.



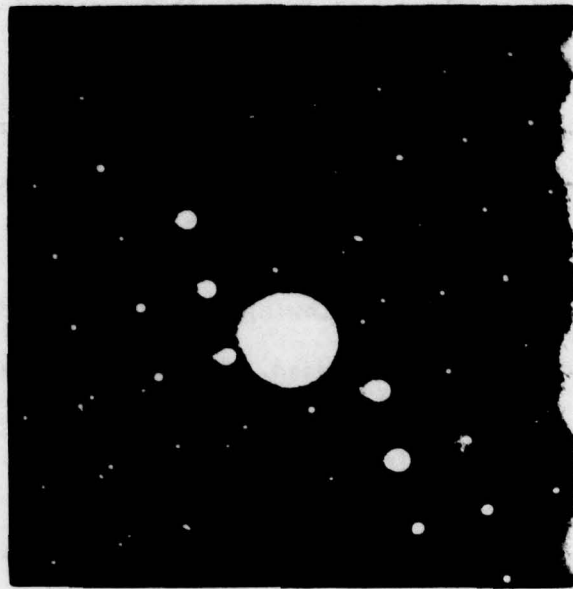


**Figure 2a.** Electron diffraction pattern of  $\text{LaB}_6$  crystal prepared by molten aluminum flux technique.

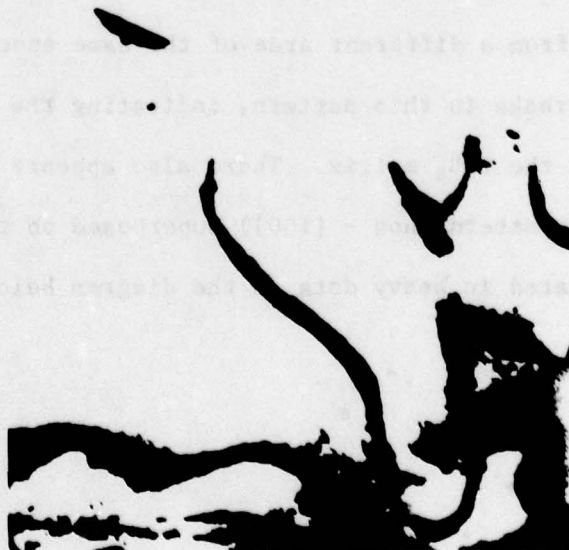


**Figure 2b.** Transmission electron micrograph of  $\text{LaB}_6$  crystal used in Figure 2a. Magnification 48,000.

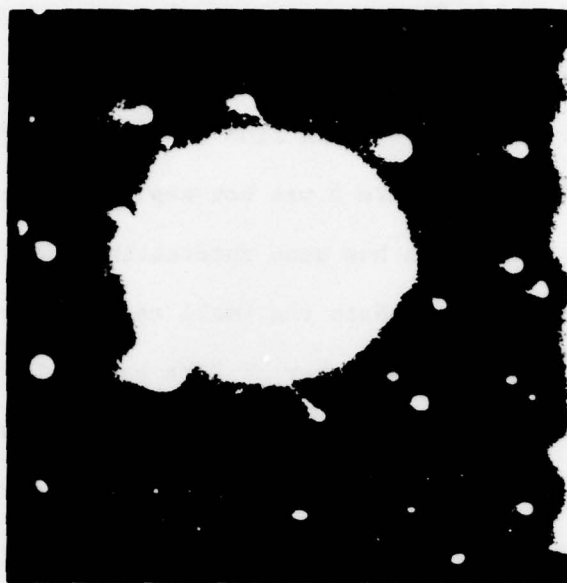


Figure 3a. Electron diffraction pattern of  $\text{LaB}_6$ . Same specimen as in Figure 2, but different area.

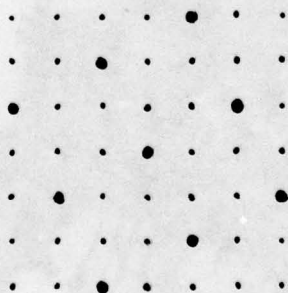


Figure 3b. Transmission electron microscope pattern of  $\text{LaB}_6$  crystal used in Figure 3a. Magnification 50,000.

Figures 4a and 4b, also from the same sample show a combination of the above two features.

Figures 5,6 and 7 were taken from a different crystal. The diffraction pattern for Figure 5 was not exposed properly and is unavailable. This micrograph has some interesting features, however, which merit its inclusion. Note the small rectangular area left of center, from which emanate a number of dark bands. This may be a microcrystal embedded in the  $\text{LaB}_6$  matrix causing a strain field to be set up in its vicinity. The dark blotchy areas on the right half and in the upper left corner may be bits of the silver paint.

Figures 6a and 6b are only approximately related due to a misalignment at the time of exposure. Notice that in this diffraction pattern and the next, that there appears to be a different relationship between the  $\text{LaB}_6[100]$  pattern and the superposed pattern than in Figures 2a, 3a, and 4a. The other pattern in this figure is also a  $[100]$  pattern.



In the micrograph there again appear to be strain fields at the lower right, and also a ring near the center.

Figure 7a shows the super-lattice as in 6a, and also a few spots indicate the presence of a grain boundary, although its presence is not clear in the micrograph.



Figure 4a. Electron diffraction pattern of  $\text{LaB}_6$ . Same specimen as in Figures 2 and 3 but different areas.



Figure 4b. Transmission electron microscope pattern of  $\text{LaB}_6$  crystal used in Figure 4a. Magnification 48,000.



Figure 5. Transmission electron micrograph from a new crystal of  $\text{LaB}_6$ . Magnification 30,000.



Figure 6a. Electron diffraction pattern of the  $\text{LaB}_6$  crystal of Figure 5.



Figure 6b. Transmission electron micrograph of the  $\text{LaB}_6$  crystal used for Figure 6a. Magnification 42,000.

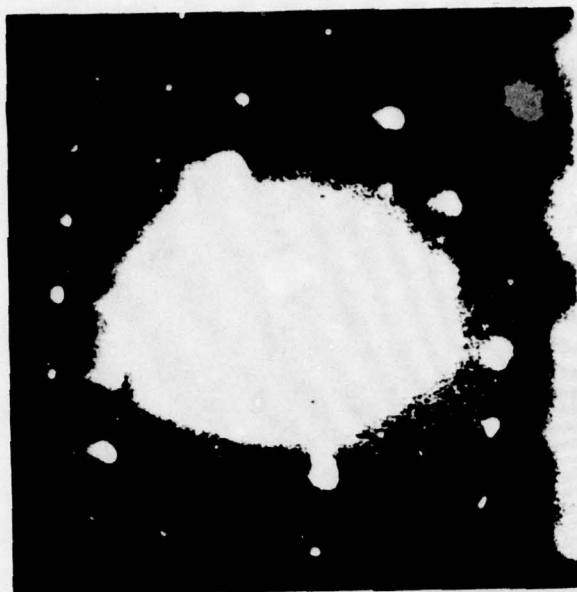


Figure 7a. Electron diffraction pattern of the  $\text{LaB}_6$  crystal of Figures 5 and 6.



Figure 7b. Transmission electron micrograph of the  $\text{LaB}_6$  crystal used for Figure 7a. Magnification 37,000.

These pictures although preliminary, do show that the crystals are not single crystals, and that a second phase or a precipitate, possibly aluminum is present.

### SECTION III

#### ELECTRON EMISSION STUDIES

##### A. Hexaborides of Lanthanum and Samarium

Two life tests of  $\text{LaB}_6$  emitters made from aluminum molten flux  $\text{LaB}_6$  crystals have been carried out, one at  $\sim 500\text{-}800^\circ\text{K}$  for 24 hours and the other at room temperature for  $90 \pm 10$  hours. In the case of the 24 hour life test the current initially was  $100 \mu\text{A}$  for emission from an emitter mounted on a Re filament in a simple diode configuration. At the end of the 24 hour period the current rose to  $> 200 \mu\text{A}$  and then went to 'zero' as determined on a chart recorder. The emitter apparently was destroyed; however on further thermal processing, a twofold symmetric pattern emerged as seen before and described in the first quarterly report. The pattern showed dark 111, 110 and 100 planes; also some indication of build-up was noticeable. An interesting feature was the presence of small bright spots indicative, perhaps, of a different surface phase such as  $\text{LaB}_4$  or some other compound of lanthanum or boron. Later experiments were performed with the  $\text{LaB}_6$  emitter operating in the TF mode at  $\sim 1500^\circ\text{K}$ ; waves of wave-like low work function material were observed spreading over the emitter. At this point, the emitter failed.

A second life test was performed on a  $\text{LaB}_6$  emitter, this time at room temperature. In this case the probe current was also monitored during the run which lasted  $90 \pm 10$  hours before emitter

failure; the uncertainty in life arises because the emitter failed at an undetermined time during a weekend run. The probe current through a 0.08 milliradians aperture was 400 nA in a background pressure of  $5 \times 10^{-9}$  torr; total current was approximately 60  $\mu$ A. Probe and total emission current Fowler Nordheim plots are shown in Figure 8. Note that the total emission current reached a maximum of 0.6 mA at 900 volts, a remarkably high value for room temperature operation.

A marked curvature is apparent in the upper end of the Fowler Nordheim plot both for probe and total current. Undoubtedly this is due to space charge effects at the emitter which become significant at the high emitter current densities occurring at the upper end of the Fowler Nordheim plots. Assuming that the average field over the emitter apex is given by  $F = V/5r$  and that only 70% of the hemispherical emitter end contributes to the emission then the current density is  $J \sim 6 \times 10^6$  A/cm<sup>2</sup> at an emission current of 0.6 mA. Close inspection of the total current Fowler Nordheim curve indicates the possibility of a break in the plot at  $\sim 300$  V. Whether this is a coincidence or a real effect remains to be elucidated.

Experiments were also performed with a third emitter, prepared from single crystals made by the molten aluminum flux technique. Photographs of the field emission patterns are shown in Figure 9a and 9b.

Figure 9a is that obtained soon after initiation of the cleaning/processing of this emitter. Notice the poorly developed

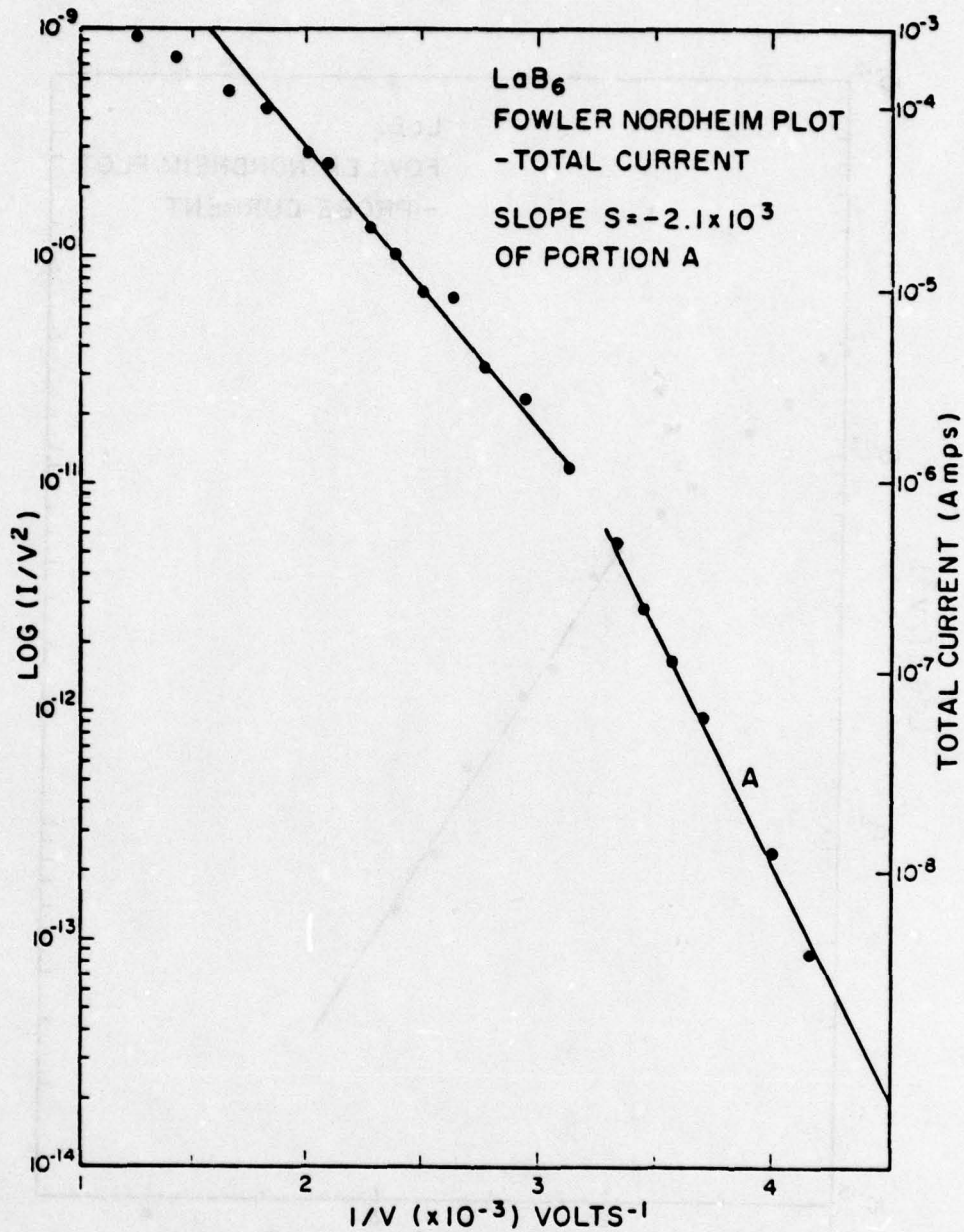


Figure 8a. Fowler Nordheim plot for a  $\text{LaB}_6$  emitter. Inset is for the probe current through a 0.08 milliradian aperture.

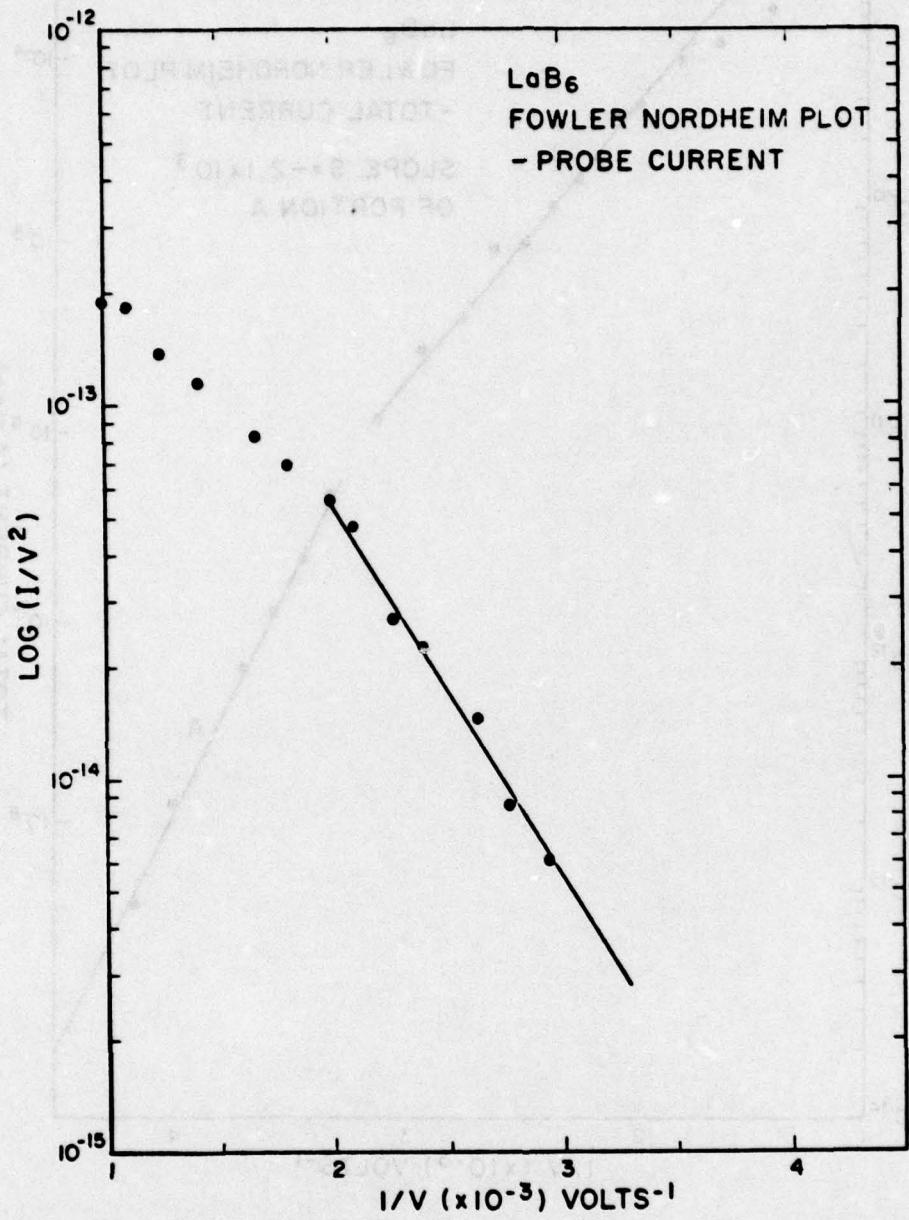


Figure 8b. Fowler Nordheim plot of probe current from a LaB<sub>6</sub> emitter.

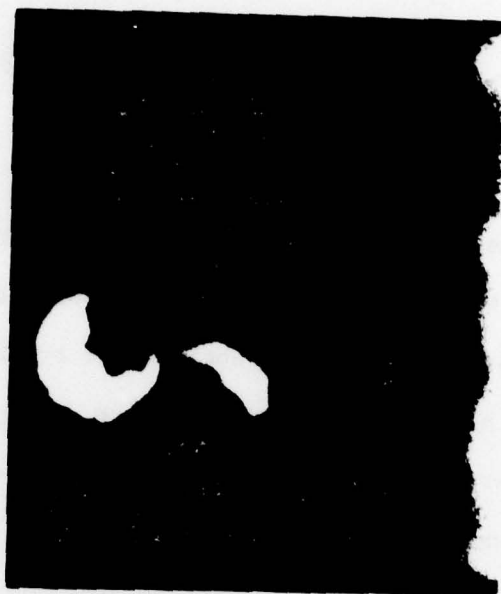


Figure 9a. Field emission pattern of  $\text{LaB}_6$  emitter made  $\text{LaB}_6$  single crystals grown by the aluminum molten flux technique. Note irregular nature of the pattern.



Figure 9b. Field emission pattern of  $\text{LaB}_6$  after repeated flashing at temperatures greater than 2000 K.

nature of the first pattern. After repeated flashing at  $> 2000$  K, the twofold symmetric pattern in Figure 9b emerged. This is typical of previous  $\text{LaB}_6$  field emission patterns.

We also examined two samarium hexaboride emitters, the first of which yielded a well ordered pattern with fourfold symmetry. This emitter was very sensitive to bombardment by gas emanating from the screen as a result of electron impact desorption. Failure of the emitter occurred soon after the beginning of experiments while the emitter was being operated in the TF mode. Another  $\text{SmB}_6$  emitter behaved in a similar manner with an initially unstructured pattern giving way finally to a fourfold symmetric pattern after being subjected to heating in the presence of a high field emission field. The final emitter voltage for viewing field emission patterns was  $\sim 6$  kV. Although field desorption at elevated temperatures was attempted in an effort to clean the emitter, no ordered pattern emerged even though the tip was dulled somewhat by the field desorption process.

Some preliminary experiments with zone melted  $\text{LaB}_6$  have been performed.

The single crystal was mounted in a holder with provision for both indirect (hot filament nearby) and direct heating by electron bombardment. After flash heating of the emitter at  $> 2000^\circ\text{K}$ , a low voltage, symmetrical pattern was obtained. Apparently, the zone melted crystals are easier to clean than those prepared by the molten flux technique.

The molten aluminum flux crystals of  $\text{LaB}_6$  seem to yield clean, symmetrical field emission patterns about 50% of the time after fairly drastic heat/field treatment when either twofold or fourfold symmetric field emission are obtained. The resulting emitters so far have been tested for periods in the range 50-100 hours.

An interesting aspect of the behavior of  $\text{LaB}_6$  field emitters is their tendency to resist dulling even when heated to temperatures close to the melting point of  $\text{LaB}_6$ . While this is an advantage in preserving the useful lifetime of the emitters at temperatures below the melting point it is probably the reason why  $\text{LaB}_6$  emitters require drastic heating regimes in order to create well ordered field emission patterns. Presumably, the low surface and bulk diffusion rates retard rearrangement of the surface layers to create surfaces of a uniform equilibrium stoichiometry. We feel that the zone melting method of preparing crystals of  $\text{LaB}_6$  offer advantages, so far confirmed by two experiments, which warrant further emphasis. In the melting process, it is much more likely that well annealed crystals, free from regions of erratic composition or of aluminum impurities will be made. The creation of a molten zone within which rapid convective mixing can occur sidesteps the difficulty of obtaining equilibrium concentrations of lanthanum and boron by annealing the molten flux  $\text{LaB}_6$  crystals for long periods.

The very high currents attainable with  $\text{LaB}_6$  emitters at room temperature is sufficient motivation to continue this work with  $\text{LaB}_6$ .

## B. Tantalum

The field emission properties of clean tantalum have been studied as a prelude to a study of the emission properties of tantalum carbide; tantalum is of interest on its own as a potential field electron emission material because of its refractory properties and because of the fact that it is adjacent in the periodic table to the much studied tungsten.

The initial field emission patterns which were obtained after flash heating of the emitter showed evidence of carbon contamination. Carbon may be easily removed from tungsten by heating it in the presence of low pressures ( $\sim 10^{-6}$  torr) of oxygen for prolonged periods. However our attempts to remove carbon from tantalum by this technique were unsuccessful. Moreover the tantalum emitter experienced considerable dulling on heating to  $\sim 1800$  K. In this respect it seems to blunt easier than tungsten.

Another aspect of the behavior of tantalum towards oxygen is the surprising insensitivity of the tantalum thermal field emission current to the presence of oxygen. Thus even at pressures as high as  $8 \times 10^{-7}$  torr of oxygen, at a tip temperature of  $\sim 1800^\circ\text{K}$ , there was no change in the emission current. Perhaps this is due to the bulk absorption of oxygen. This would also explain the lack of effect of oxygen on the surface carbon contamination.

The build-up<sup>3</sup> properties of tantalum are a source of interest because both tungsten and molybdenum - close neighbors of tantalum in the periodic table, exhibit interesting build-up phenomenon. In particular the build-up<sup>4</sup> of (100) oriented tungsten emitters provides a very important practical high brightness TF electron source.

A preliminary look at the build up behavior of tantalum was obtained on the somewhat carburized emitter described above. Although the field emission patterns obtained were significantly different than those reported for clean tantalum, the emitter radius decreased by 43% during build-up at 1800 K. The built-up patterns showed considerable emission from the 311-211 region in addition to the enhanced emission from the 111 region whereas for the clean built up emitter, emission was largely confined to the 111 planes.<sup>4</sup>

### C. Iridium

Build-up studies were also performed on a slightly contaminated (100) oriented iridium emitter. The ratio of built-up radius to thermally annealed was found to be 0.543 as determined by the slopes of the Fowler Nordheim plots. The build up seems to occur on the 110 plane and seems to be accompanied by the development of 100 and 111 facets. Photographs of the thermally annealed and built-up field emission patterns are shown in Figures 10a and 10b. The ring around the 100 plane is due to slight contamination of the emitter. An examination of the kinetics of the build up phenomenon was carried out by measuring growth of the field emission current as a function of temperature at a constant voltage. An Arrhenius plot of the build-up is shown in Figure 11. Also shown in Figure 12 for comparison is an earlier unpublished study of the field build-up kinetics for tungsten. It is worthwhile to note that the field increases during build-up since the radius of the built-up emitter is approximately 50% less than at the beginning.

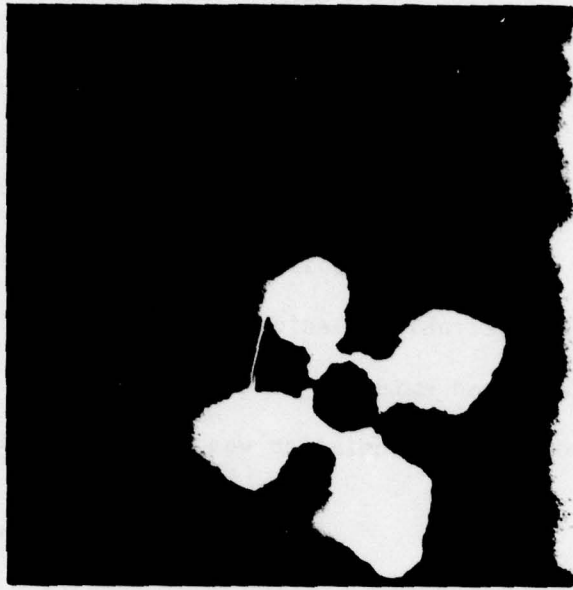


Figure 10a.



Figure 10b . Field emission patterns of a thermally annealed (Figure 10a) and built-up (Figure 10b) iridium field emitter.

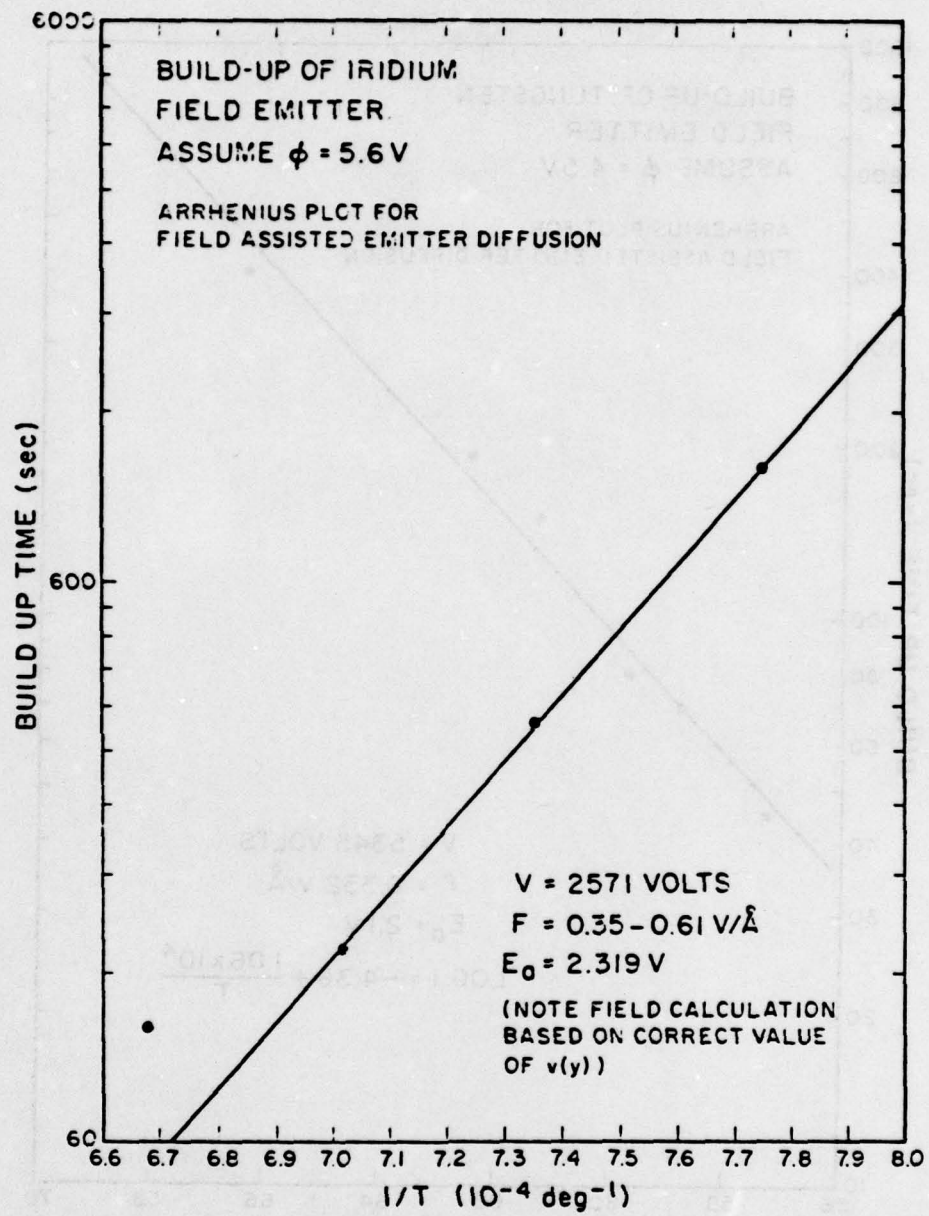


Figure 11. Arrhenius plot for field assisted surface diffusion of iridium.

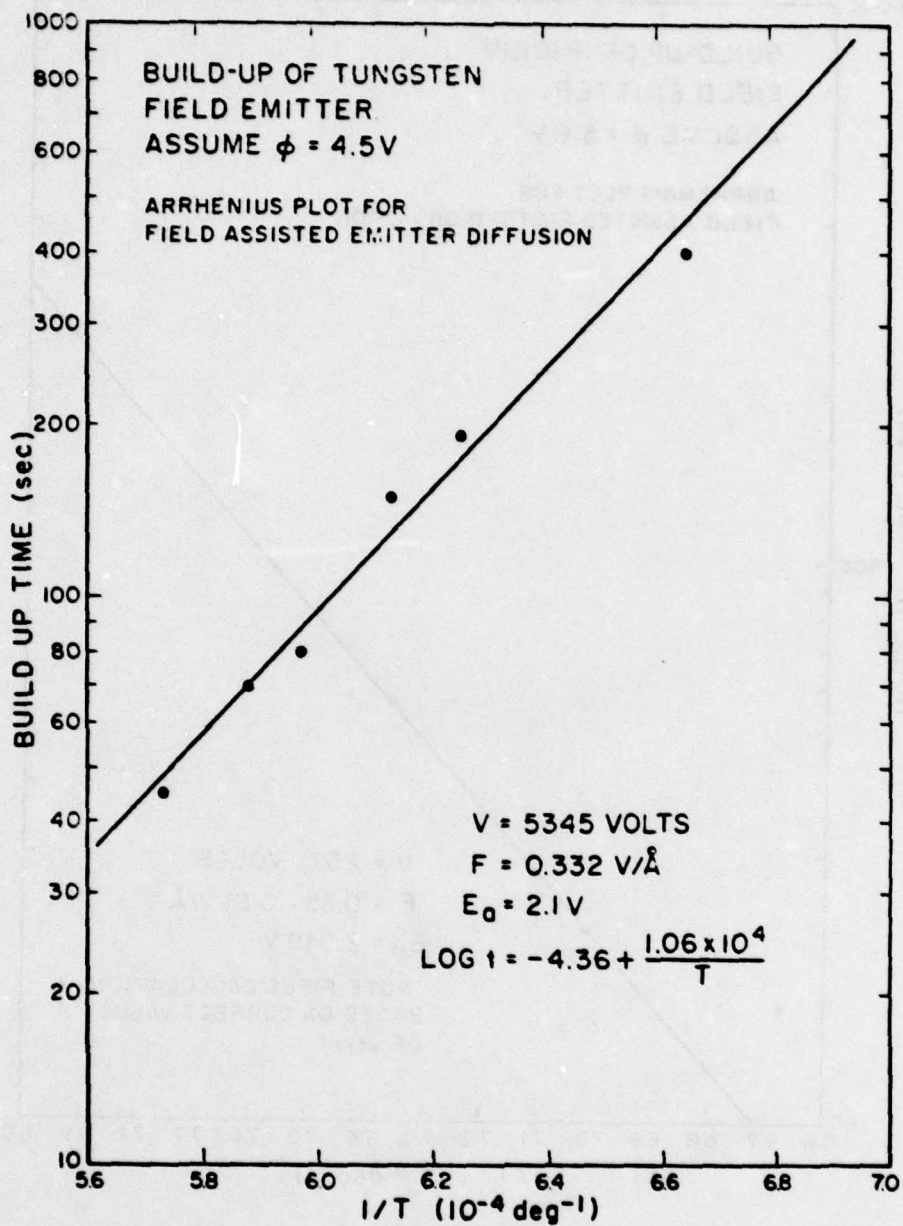


Figure 12. Arrhenius plot for field assisted surface diffusion of tungsten.

In spite of this reasonable Arrhenius plots were obtained and both for tungsten and iridium the activation energies for field assisted diffusion were 2.1 eV and 2.3 eV respectively. An earlier activation energy for field build-up of tungsten was obtained<sup>5</sup> by Bettler and Charbonnier who obtained an activation energy for tungsten of 2.44 eV. Field free diffusion activation energies have also been obtained for tungsten<sup>6</sup> and are considerably greater at an average value of 3.0 eV. The difference of approximately 0.6 eV between the field-free and the field assisted surface diffusion rates also presumably applies to iridium which by analogy would have a field free diffusion energy of ~ 3.0 eV. This compares with a value of 2.3 eV obtained by Bettler and Barnes.<sup>7</sup> Melmed,<sup>8</sup> examined two other close packed metals - Pt and Ni and found no difference between field-free and field assisted build-up. Possibly there is a difference in behavior between the close packed and body centered metals with respect to diffusion properties.

#### D. Field Emission Total Energy Distribution (TED)

##### 1. Introduction

It is of interest to have knowledge of the energy distribution of field emitted electrons because of the limiting effect this has on focussed spot size. For example,<sup>9</sup> in a cylindrically symmetric lens spherical and chromatic aberrations produce an image consisting of circles of radius  $r'_s$  and  $r'_c$  slightly ahead of the gaussian image plane, where

$$r'_s = (1/4)MC_s \alpha^3 \quad (1)$$

$$r'_c = (1/2)MC_c (\Delta E/E)\alpha \quad (2)$$

and  $M$  is magnification of the lens,  $C_s$  is the spherical aberration coefficient referred to the object space,  $C_c$  is the chromatic aberration coefficient and  $\alpha$  is the angle of the ray leaving the object which passes through the aperture;  $\Delta E$  is the energy spread of the electron beam of energy  $E$ . Combining  $r'_s$  and  $r'_c$  in quadrature we have, the spot radius  $r$ :

$$r = (M\alpha/2) \left[ C_c^2 (\Delta E/E)^2 + C_s^2 \alpha^4/4 \right]. \quad (3)$$

Clearly we need to know  $\Delta E/E$  if we wish to estimate spot size;  $\Delta E$  may be obtained by determining the full half width maximum (FHWM) of the TED and in this report we discuss measured and calculated values of  $\Delta E$  for emitters at temperatures in the range 377-2000°K.

Field emission electrons may be extracted from metals when fields,  $F$ , of the order  $10^9 - 10^{10}$  volts/meter are applied to the emitter. Electric fields of this magnitude deform the metal electron potential energy curve so that electrons, at the highest level in the metal - the Fermi level, are presented with a potential barrier through which they are able to tunnel in appreciable amounts.

The TED for such electrons, in the free electron approximation, is given by<sup>10</sup>

$$j(\epsilon) = \left[ (4\pi me)/h^3 \right] f(\epsilon) \int_0^{\epsilon + E_F} D(W) \cdot dW \quad (4)$$

where  $m$  and  $e$  are the mass and charge respectively of an electron in the metal,  $h$  is Plank's constant;  $\epsilon$  is the total electron energy, measured relative to the Fermi level which is above the bottom of the metal conduction band by an amount  $E_F$ .  $f(\epsilon)$  is the Fermi function

$f(\epsilon) = [1 + \exp(\epsilon/kT)]^{-1}$  where  $k$  is the Boltzmann constant and  $T$  is absolute temperature;  $W$  is the part of the energy for the motion perpendicular to the surface:

$$W = [p^2(x)/2m] + V(x) \quad (5)$$

where  $p(x)$  is the electron momentum normal to the surface, and  $V(x)$  is the effective electron potential energy. The function  $D(W)$  is the probability that an electron incident on the barrier will emerge from the metal and is obtained by solution of the Schrödinger equation:

$$\frac{d^2\psi}{dx^2} + \frac{2m}{\hbar^2} [W - V(x)]\psi = 0 \quad (6)$$

From the WKB approximation  $D(W)$  is obtained from:

$$D(W) = [1 + \exp(A(W))]^{-1} \quad (7)$$

where  $A(W)$  is given by:

$$\begin{aligned} A(W) &= (4/3)(2m/\hbar^2)^{1/2} \cdot (E_F + \phi - W)^{3/2} \cdot v(y)/(eF) \\ &= 0.6829 \cdot (E_F + \phi - W)^{3/2} \cdot v(y)/F \end{aligned} \quad (8)$$

where  $F$  is given in  $V/\text{Å}$  and  $E_F$ ,  $\phi$ ,  $W$  are measured in volts;  $y$  is given by

$$\begin{aligned} y &= (e^3 F)^{1/2} / (E_F + \phi - W) \\ &= 3.79 F^{1/2} / (E_F + \phi - W) \end{aligned} \quad (9)$$

Murphy and Good<sup>11</sup> have derived expressions for  $v(y)$ :

$$v(y) = (y/2)^{1/2} \{2E(k_1) - (y+1)K(k_1)\} \quad y > 1 \quad (10)$$

$$v(y) = (1+y)^{1/2} \{E(k_2) - yK(k_2)\} \quad y < 1 \quad (11)$$

$$\text{and } k_1 = (y - 1/2y)^{1/2}; \quad k_2 = \{(1-y)/(1+y)\}^{1/2} \quad (12)$$

E and K are the standard elliptic functions:

$$E(k) = \int_0^{\pi/2} (1 - k^2 \sin^2\theta) \cdot d\theta; \quad K(k) = \int_0^{\pi/2} (1 - k^2 \sin^2\theta)^{-1/2} \cdot d\theta \quad (13)$$

In the work presented here, the integral in Equation 4, was integrated numerically using the well known Simpson's rule which involves evaluation at equally spaced intervals h of the function to be integrated:

$$I = \int_a^b f(x) \approx S(N) = f(a) + 4 \sum_{m=1}^{2^{N-1}} f[a + (2m - 1)h] + 2 \sum_{m=1}^{2^{N-1}-1} f[a + 2mh] + f(b) \quad (14)$$

where h is given by

$$h = (b - a)/2^N$$

The summation 14 is usually repeated at increasing values of the integer N beginning at N = 1 until two successive values of S(N) differ less than a specified amount - in this case by part in  $10^6$ . A more economical method of obtaining accurate estimates of I may be obtained by using the Romberg extrapolation to technique which greatly limits the necessary number of subdivisions of h required. Thus an improvement S(N,J) in the estimate of I may be obtained by using the extrapolation formula:

$$S(N,J) = \frac{4^{J-1}S(N+1, J-1) - S(N, J-1)}{4^{J-1} - 1} \quad (15)$$

where  $S(N+1, J-1)$ ,  $S(N, J-1)$  are previous Simpson or Romberg extrapolated values.

## 2. Calculated Values of Full Width Half Maxima

In order to evaluate the FWHM, it is first necessary to locate the peak in the TED function (Equation 4) and then to search out for the abscissa values corresponding to the half maximum ordinates.

This was performed as a function of field for two work functions -  $\phi = 2.5$  eV,  $\phi = 4.5$  eV and for a range of temperatures 78°K - 1800°K; the results are shown in Figures 13 and 14.

A remarkable feature of all these curves is the sharp maximum in the curve which occurs at fields in the range 0.1 - 0.4 V/Å. The 4.5 eV work function curves show the most pronounced maxima which increase with temperature, reaching a maximum of ~ 2 eV at a temperature of 1500°K and a field of 0.25 V/Å. At higher fields than that corresponding to the maximum, the FWHM declines from ~ 2 eV at  $F \approx 0.25$  eV to a value of ~ 0.7 eV at fields in the range 0.5 - 0.7 V/Å. At higher fields the FWHM slowly increases. The minimum occurring beyond the maxima show a steady increase with temperature from ~ 0.27 eV at 600°K to ~ 0.75 eV at 1800°K, hence the minima is approximately proportional to T. The field shift of the maxima and minima with temperature is also of interest; both maxima and minima decrease to lower fields as temperature decreases, also the maximum rapidly diminishes as temperature declines below

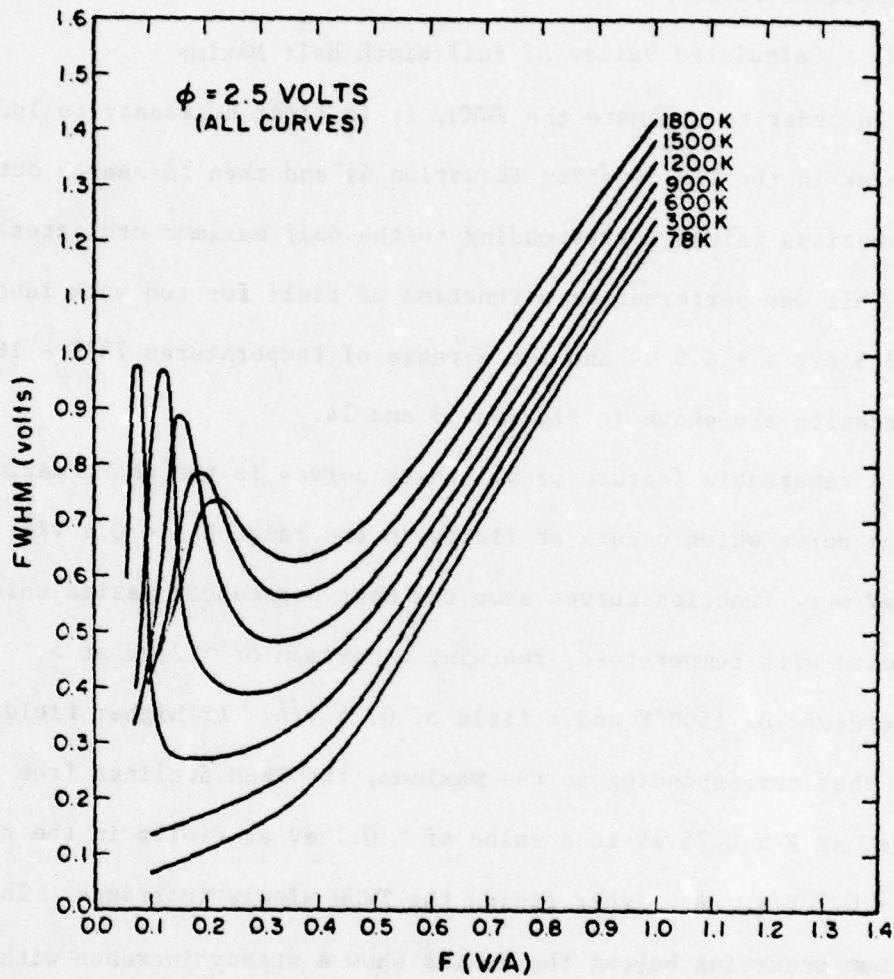


Figure 13. Plot of the full-width at half maximum (FWHM) for the energy distribution of field emitted electrons as a function of electric field  $F$  at various temperatures;  $\phi = 2.5$  V.

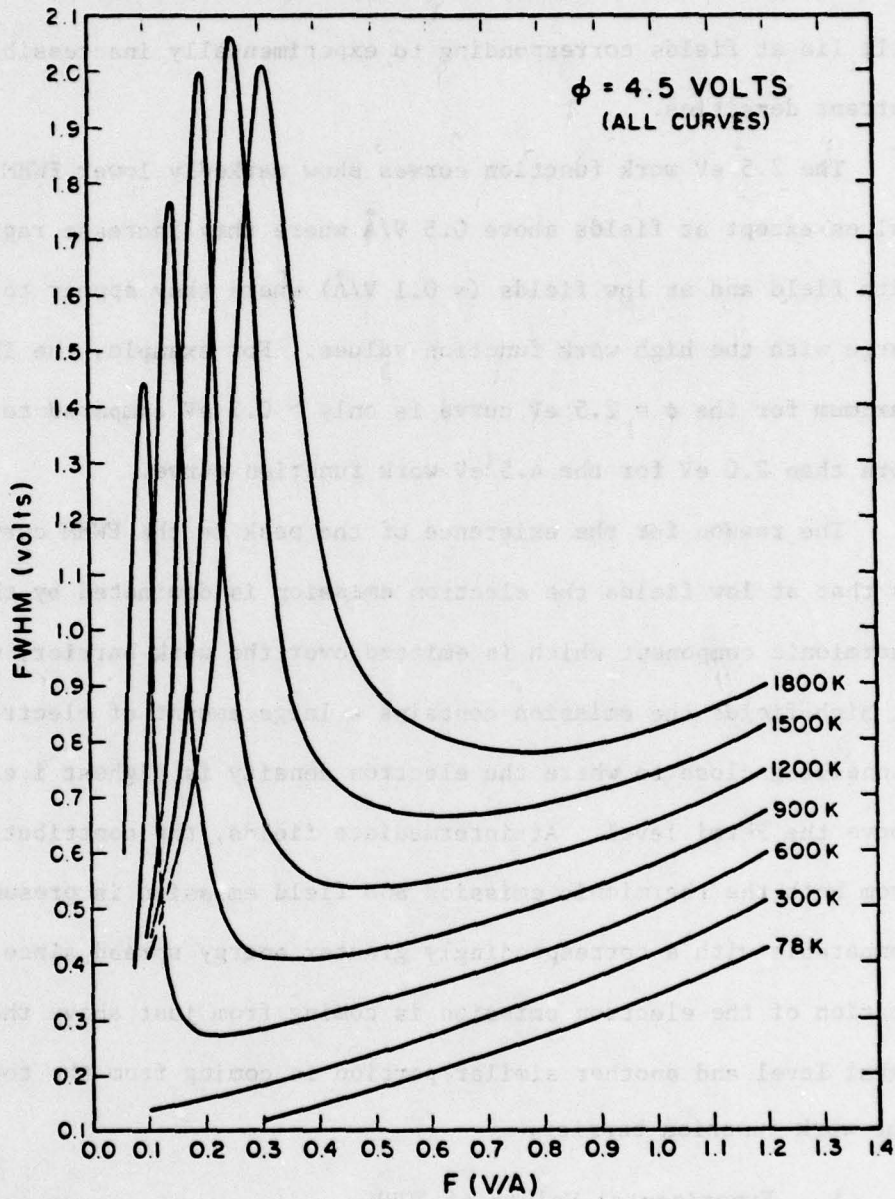


Figure 14. Plot of FWHM for the energy distribution of field emitted electrons as a function of electric field  $F$  at various temperatures;  $\phi = 4.5$  V.

300°K; at this temperature, the position of the maximum has shifted to less than 1 V/Å. Clearly for temperatures below 300°K, the maxima will lie at fields corresponding to experimentally inaccessible current densities.

The 2.5 eV work function curves show markedly lower FWHM values except at fields above 0.5 V/Å where they increase rapidly with field and at low fields ( $< 0.1$  V/Å) where they appear to converge with the high work function values. For example, the 1800°K maximum for the  $\phi = 2.5$  eV curve is only  $\sim 0.7$  eV compared to more than 2.0 eV for the 4.5 eV work function curve.

The reason for the existence of the peak in the FWHM curve is that at low fields the electron emission is dominated by the thermionic component which is emitted over the work barrier, while at high fields the emission contains a large amount of electrons tunnelling close to where the electron density is highest i.e., just above the Fermi level. At intermediate fields, the contribution from both the thermionic emission and field emission is presumably comparable with a correspondingly greater energy spread since a portion of the electron emission is coming from just above the Fermi level and another similar portion is coming from the top of the work function barrier.

### 3. Experimental Values of FWHM

Experiments have been performed at various temperatures with two emitters, a zirconiated (100) oriented W emitter and a built-up (100) oriented W emitter. The energy analyzer used was a concentric

sphere retarding potential analyzer with a limiting aperture of 0.975 milliradian; a cross section of the analyzer is shown in Figure 15. This analyzer does not use the focussing cross-over present in, for example, the Van-Oostrom retarding potential analyzer. In previous<sup>12</sup> experiments at 90°K with the latter analyzer, FWHM values considerably larger than calculated values were measured. It was speculated that this was due to space charge broadening occurring in the cross-over region. Hence the use of an analyzer which did not have such a cross-over such as the concentric sphere analyzer would resolve this question. The results with the concentric sphere analyzer repudiated the "cross-over" theory because the experimentally determined FWHM values from this analyzer shown in Figures 16 and 17 are considerably larger than the theoretical values everywhere, except at one field and temperature value. The very rapid increase in FWHM at high fields also occurred in the data obtained from the cross-over analyzer. At  $T = 1750$  K,  $F = 0.34$  V/A and  $\phi = 4.5$  V, the calculated FWHM is  $\sim 1.3$  eV compared to the experimental value of  $\sim 1.1$  eV. Since the calculated values of FWHM are clearly very sensitive to field in this region, a slight error in the experimentally determined value of field could easily account for the discrepancy. It would be interesting to experimentally examine further the low field region of the FWHM curves to verify the existence of the peak. For the 2.6 eV work function experimental curve, the field range examined straddles the field values corresponding to the theoretical peak which has a maximum value of

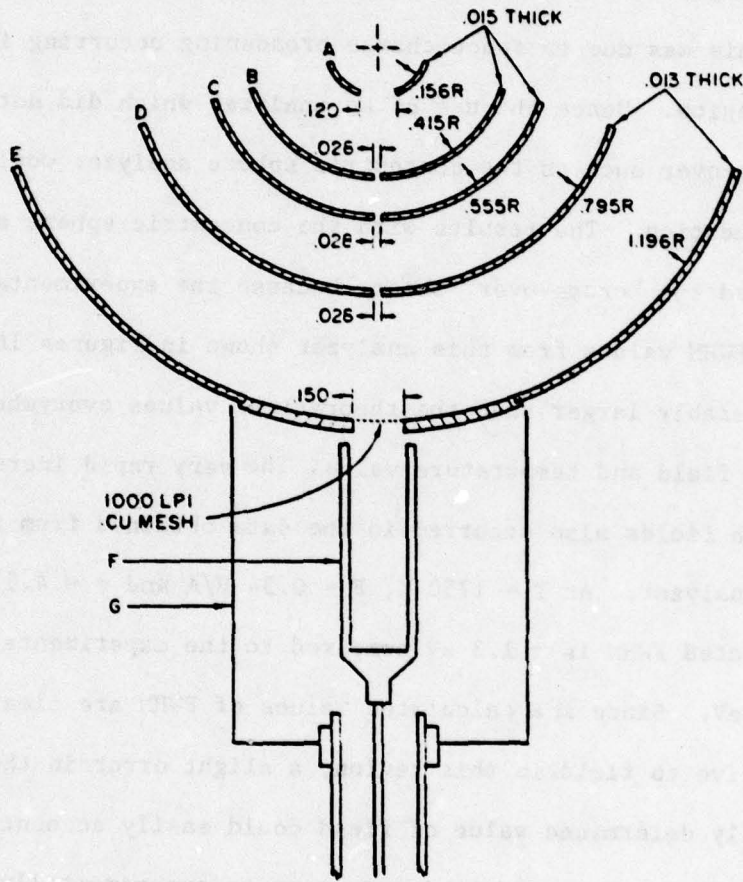


Figure 15. Cross section of the concentric sphere retarding potential analyzer.

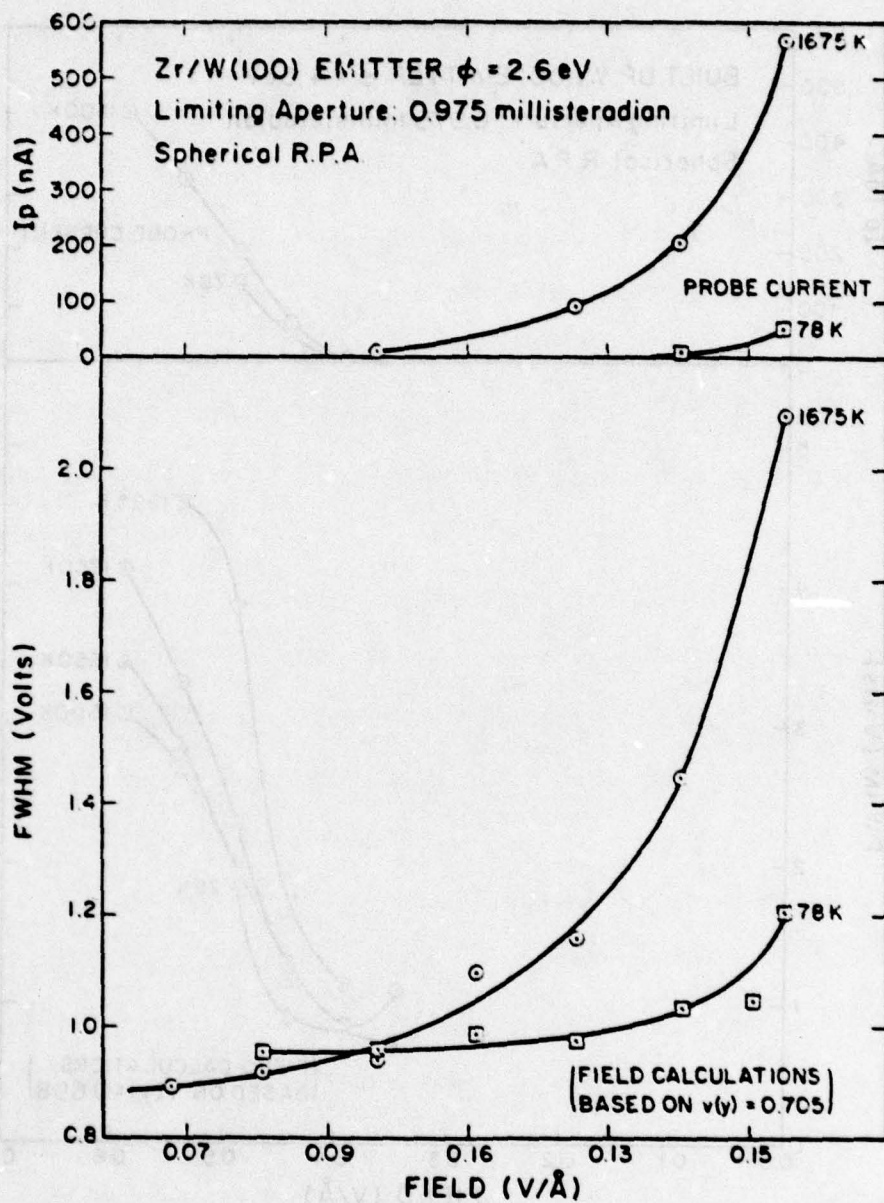


Figure 16. FWHM and probe current versus electric field at 78°K and 1675°K for zirconiated tungsten.

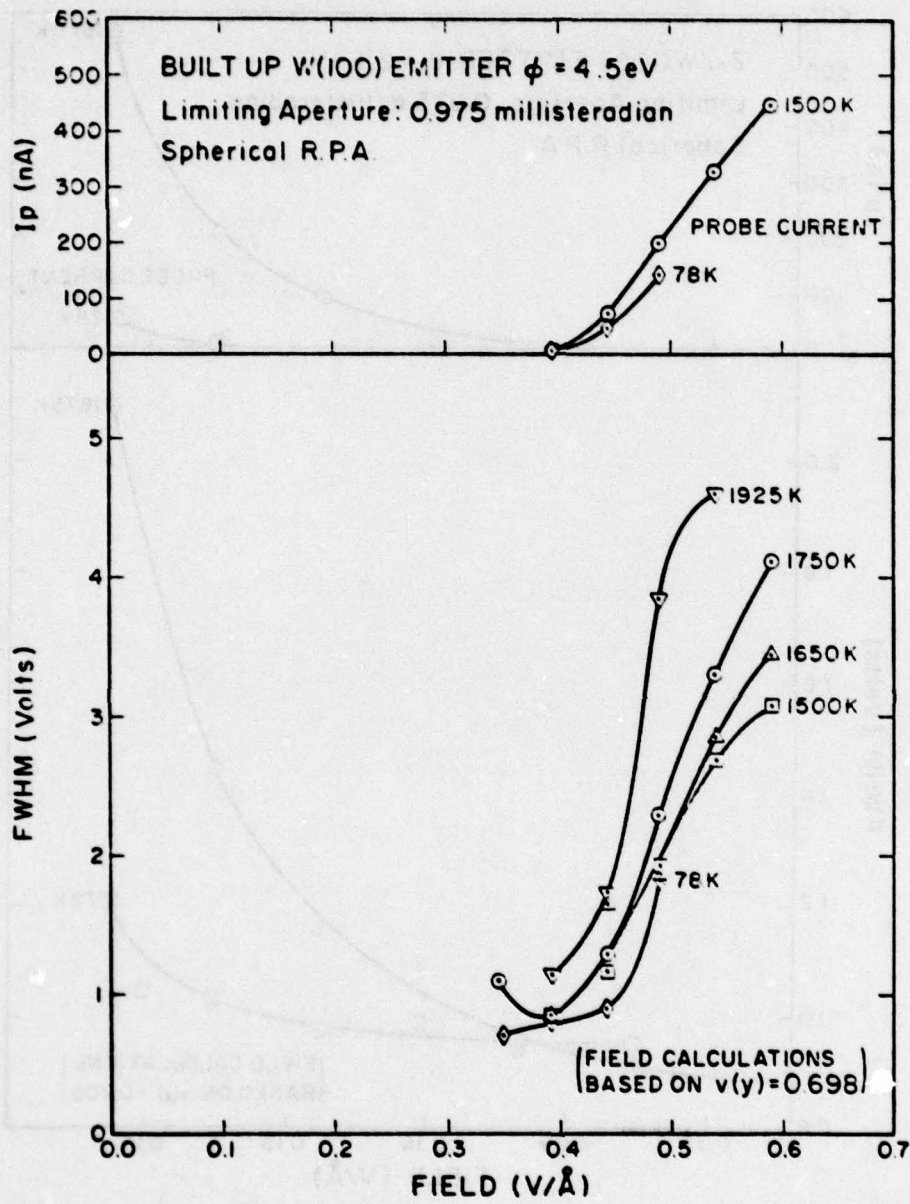


Figure 17. FWHM and probe current versus electric field at various temperatures for a built-up tungsten field emitter.

0.7 - 0.8 eV compared to the low field experimental value of  $\sim 0.9$  eV. Apparently the resolution of the present analyzer was not good enough to uncover the peak predicted by theory.

The most striking aspect of the experimental values of FWHM, both at  $\phi = 4.5$  eV and at  $\phi = 2.6$  eV, is the very large values of FWHM which occur at probe currents above  $\sim 100$  nA. For both work function values, the discrepancy between theoretical and experimental values of FWHM with probe current suggests a space charge broadening effect of some kind. We hypothesize here that the increase in energy spread of the probe current is due to space charge broadening occurring at the emitter surface where the electron velocity is low.

The present experimentally determined values of FWHM for the zirconiated (100) oriented emitters agree well with previously<sup>12</sup> determined values. Although the field values do not agree, that is because in the present work, fields have been calculated on the basis of correctly calculated  $v(y)$  values whereas in the earlier work it was assumed that  $v(y) = 1$  instead of 0.7; earlier values of field must be multiplied by 0.7.

For the built-up (100) oriented emitter, however, the FWHM values were considerably larger than earlier results at the maximum fields investigated. Thus the maximum FWHM at 1650 K in the present work is  $\sim 3.5$  V compared to  $\leq 2$  V obtained previously at 1600 K. Apart from the different types of energy analyzers used, the major difference in the two apparatus used for energy analysis is the size

of limiting aperture used. In the present work the aperture is 0.98 milliradian compared to 0.079 milliradian in the previous work.<sup>12</sup> We speculate that this results in a significant increase in the FWHM only for the built up emitter because of the very small effective emitting area of the built emitter which has a chisel like geometry. If the acceptance angle of the analyzer is large enough, emission from the sides of the emitter will be accepted. Since this emission originates from a surface of a slightly different orientation than the (100) direction and because it is directed away from the analyzer direction, significant broadening of the FWHM can be expected.

The FWHM results are significant because of their effect on electron beam spot size. Most spot sizes are chromatic limited so that information concerning FWHM can have a major impact on strategies to minimize spot sizes. Apparently the built-up emitters will require smaller apertures for best results.

## SECTION IV

### FIELD IONIZATION STUDIES

#### A. Apparatus Description

We have used a previously built optical column to measure FI source properties. The purpose of this was to confirm earlier measurements under conditions similar to those which would be met in the memory writing system.

A scanning ion microprobe (SIM) was constructed with a commercial pumping station to provide the necessary vacuum. The optical system consists of two electrostatic lenses, an objective aperture, electrostatic beam steerers and a double deflection beam scanning system with two sets of electrostatic plates for the X and Y directions, respectively. The first lens (objective) is located just below the ion source and the final lens (projector) just above the specimen.

The lenses are arranged as a doublet (see Fig. 18). The objective collimates the beam forming an image at  $z = \infty$  of size  $d_1 = 2r_1$ ,

$$r_1 = M \left( \rho^2 + \left( \frac{1}{2} C_{s1} \alpha^3 \right)^2 + \left( \frac{1}{2} C_{c1} \frac{\Delta V}{V} \alpha \right)^2 \right)^{1/2}. \quad (16)$$

$M$  is the magnification,  $C_{s1}$  the spherical aberration coefficient and  $C_{c1}$  the chromatic aberration coefficient.  $\Delta V$  is the energy spread of the beam,  $V$  the acceleration voltage,  $\alpha$  is the angular divergence of the beam as determined by the objective aperture, which has a diameter of 0.13 mm and  $\rho$  is the apparent source size. The projector lens focusses the collimated beam on the specimen at

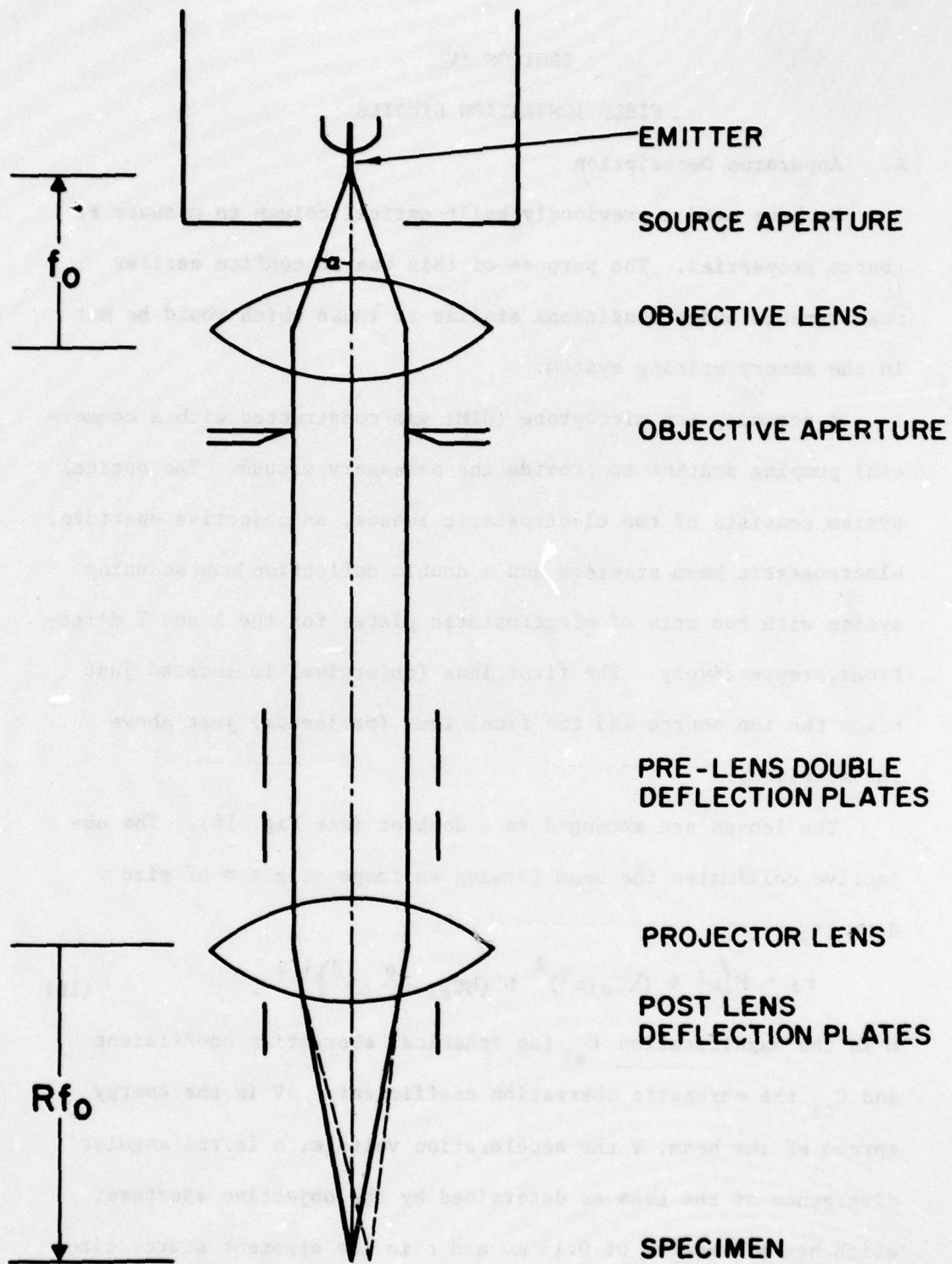


Fig. 18. Schematic diagram of the SIM optical system, with FI source at the top. Typical values for  $f_0$  are 5-9 mm and  $R = 9-5$  ( $R$  is dimensionless).

a working distance of  $\approx R f_o$ , where  $f_o$  is the objective lens focal length  $\approx 5$  mm,  $R$  is the ratio of projection and objective lens focal lengths and the amount of demagnification is  $M' = \frac{R}{M}$ . The overall magnification is  $MM' = R$ . The diameter of the beam on the specimen is  $d_2 = 2r_2$ , where

$$r_2^2 = M'^2 r_1^2 + \left( \frac{1}{2} C_{s2} \left( \frac{\alpha}{R} \right)^3 \right)^2 + \left( \frac{1}{2} C_{c2} \frac{\Delta V}{V} \frac{\alpha}{R} \right)^2 \quad (17)$$

Using the values  $f_{obj} = 5.5$  mm,  $C_{s1} \approx 88$  mm,  $C_{s2} \approx 4000$  mm,  $C_{c1} \approx 18$  mm,  $C_{c2} \approx 150$  mm,  $\rho \approx 10$  Å,  $\Delta V \approx 4$  eV (for  $H_2^+ + H^+$ ),  $V = 12$  kV, and  $\alpha = 0.012$  and  $R = 6$  then  $d_2 = 6300$  Å. The effect of the aberration terms of the projector or lens are negligible:

$$\left( \frac{\frac{1}{2} C_{s2} \left( \frac{\alpha}{6} \right)^3}{M' r_1} \right)^2 = 6 \times 10^{-4}; \quad \left( \frac{\frac{1}{2} C_{c2} \frac{\Delta V}{V} \frac{\alpha}{6}}{M' r_1} \right)^2 = 2.5 \times 10^{-2} \quad (18)$$

so that the overall contribution of the projector lens to the aberration disc of confusion is only 2%.

The objective aperture is a standard 130  $\mu$ m platinum aperture available commercially for use in electron microscopes. The optical components are mounted in a tube 38 cm long which can be removed from the SEM without affecting the alignment of the components. The lens tube is held rigidly in a vacuum column fitted with a number of feed-throughs for making electrical connections as shown in Fig. 19.

The ion source described above is shown in Fig. 20. It is mounted in an X-Y traversing stage controlled by two 0.00025 cm resolution micrometers. The micrometers are located at the ends of lever arms with the gun halfway between them and the pivot points, so that the motion of the gun is one-half that of the micrometers, i.e., the gun

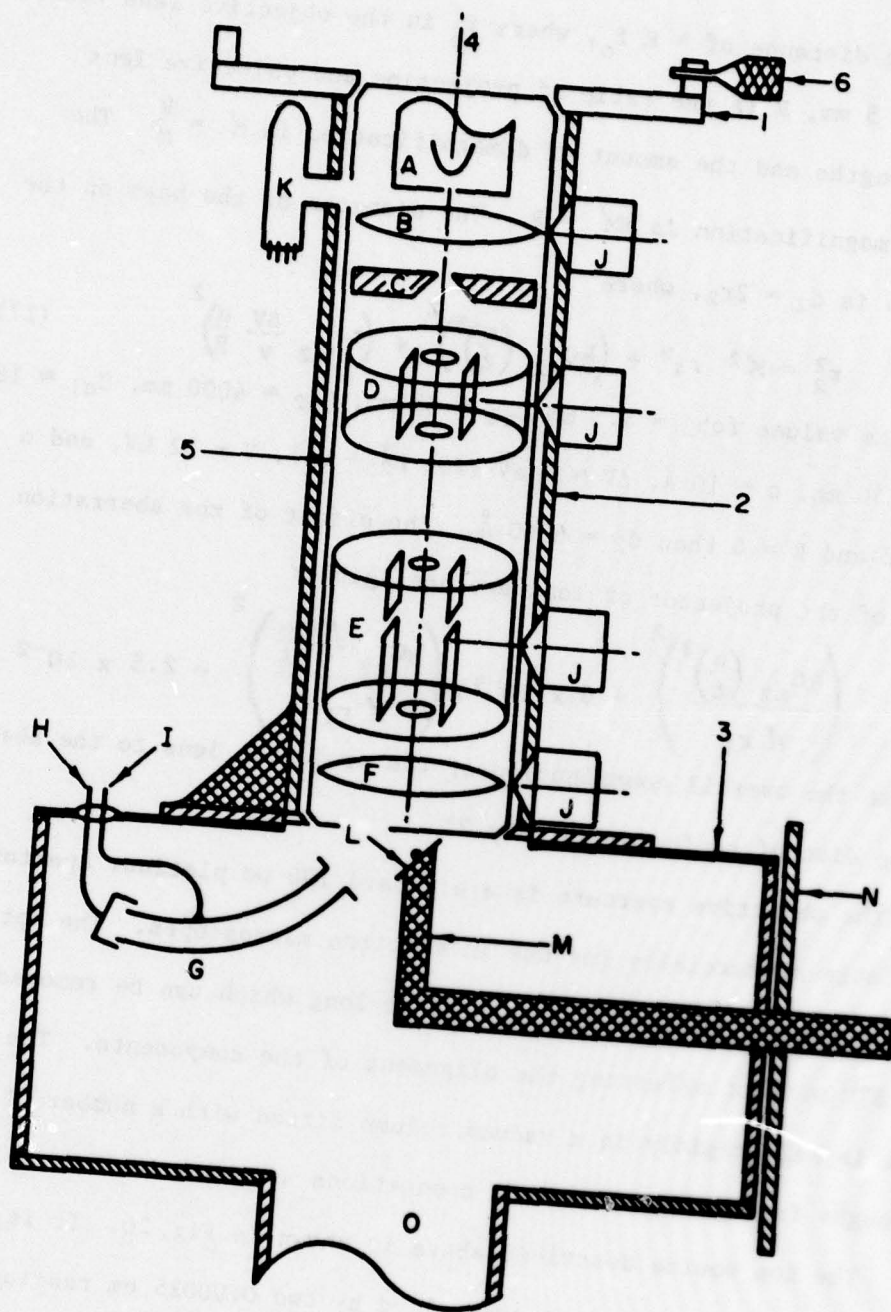


Fig. 19. Schematic diagram of the SIM (see legend following).

LEGEND FOR FIGURE 19

1. Ion source traversing stage
  2. Vacuum column
  3. Specimen chamber
  4. Optical axis
  5. Lens tube
  6. Micrometer
- 
- A. FI source
  - B. Objective lens
  - C. Objective aperture
  - D. Beam steering plates
  - E. Beam deflection plates
  - F. Projector lens
  - G. Channeltron secondary electron detector
  - H. Signal output
  - I. High voltage input
  - J. Electrical feedthroughs
  - K. Ionization Gauge
  - L. Specimen
  - M. Specimen holder
  - N. Vacuum door holding specimen manipulators
  - O. Vacuum port

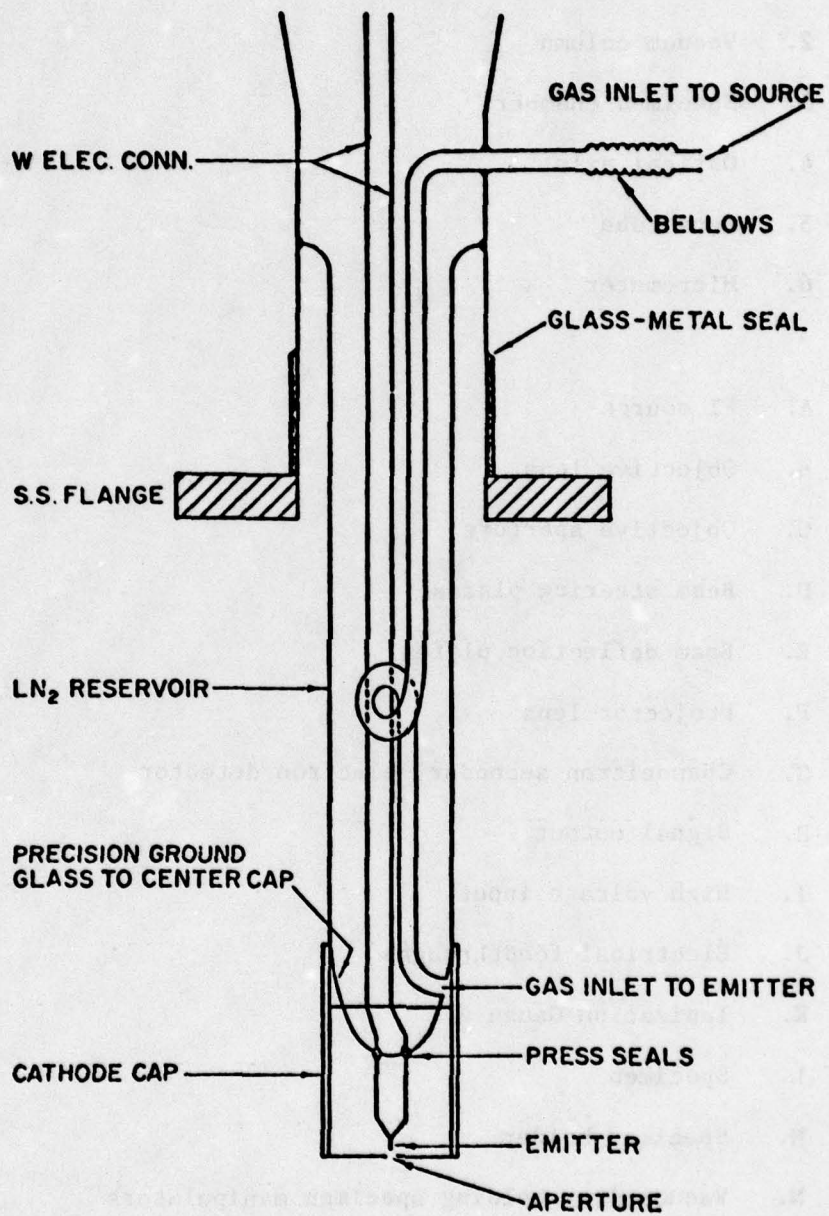


Fig. 20. Drawing of the FI source which was used by technician to build present unit. Aperture size is 0.5 mm, emitter-aperture spacing 0.5 - 1.5 mm.

can be moved in 0.00013 cm increments. When the gun is aligned for maximum current on the specimen a movement of the gun by 0.005 cm (50  $\mu\text{m}$ ) will alter the image location so that no current strikes the specimen.

The double deflection beam scanner is located 77 mm below the objective aperture and has a 1 mm aperture at the top. The scanner is driven by a set of four high voltage operational amplifiers controlled by a two channel ramp generator. For ordinary viewing the beam is driven at  $\sim 1$  Hz in the x-direction and 100 Hz in the y-direction. The sweep rate can be slowed for photography to ensure that the resolution of the monitor is not exceeded. Just under the beam deflector there is a movable beam stop on which the beam can be intercepted to read the specimen current. The stop is biased +20 volts with respect to ground to suppress secondary electrons.

An ionization gauge is located  $\approx 5$  cm from the ion gun. The base pressure at that point is  $2-5 \times 10^{-6}$  torr. When gas is allowed into the gun the pressure rises to between 0.9 and  $3 \times 10^{-5}$  torr, depending on how much current is desired and the type of gas being ionized.

The high voltage for the SIM is provided by a regulated power supply which also energizes the electrostatic lenses. In order to vary the lens focal lengths the voltage applied to them must be variable. This is accomplished by connecting the lenses to the high voltage through a 1000 M $\Omega$  voltage divider. In addition, potentiometers can be connected across the high voltage divider for fine focus control.

A "floating" nanometer is connected in series with the lead to the FI source so the total current can be measured. All the electrical connections to the SIM are shielded by grounded braid.

Secondary electrons produced when the beam strikes the specimen are detected by a high gain channeltron detector. The signals produced by the multipliers are amplified and the contrast modified slightly by a bias circuit before being fed to the Z axis (intensity control) of the CRT monitor to modulate the intensity.

A simple three-axis stage is used to hold the specimen. The stage is controlled by three micrometers with 10  $\mu\text{m}$  resolution.

The gas inlet system for the gun consists of a Pd hydrogen purifier connected to a manifold where other gas bottles may be attached. Gas is leaked into the gun via finely controlled Granville-Phillips valve. The manifold has provision for independent pumping to ensure gas purity.

Because of the optical design in which the overall magnification of the source is of the order of unity, pains have been taken to decouple the microprobe from building vibration.

Vibrational amplitude  $\sim 3000 \text{ \AA}$  would be magnified to cause a beam displacement of 1  $\mu\text{m}$  on the specimen. The estimated frequency of vibration of the field emitter mounted on a 0.010" W loop is  $\sim 20$  kHz. Since the vertical scan rate is typically 100 Hz the result of such vibration would be to cause a loss of resolution along the direction of the emitter motion. The gas supply is fixed firmly to the frame of the instrument and the whole SIM is mounted on springs with a  $\sim 1$  Hz resonant frequency. No motion of the emitter is visible under a

500X light microscope with the gun resting on a table. A sharp tap on the glass portion of the gun excites no discernable vibration.

#### B. Results - Field Ionization Current/Voltage Data

The microprobe has been operated primarily with hydrogen gas at a pressure of  $\approx 10^{-2}$  torr and with a field of  $\approx 2$  volts/Å on Ir emitters formed from polycrystalline wire. The applied voltage varies from 10 kV to 20 kV, depending on the emitter radius. A typical current-voltage curve for the gun is shown in Fig. 21, where probe current refers to the current measured just above the specimen.

The objective aperture subtends a solid angle of 0.45 msr when the objective lens is properly focussed to produce a collimated beam with a 5 mm focal length. Under these conditions, with a source sensitivity of  $5 \times 10^{-5}$  A/sr torr the expected probe current is  $2 \times 10^{-10}$  amperes with  $P_{H_2} = 1 \times 10^{-2}$  torr.

Because of the optical system employed the current on the specimen is not affected by the focal length of the final lens. As the specimen is moved closer to the lens and its focal length is shortened the overall magnification of the source by the two lenses is lessened and the beam spot size reduced. Thus the current is independent of the resolution for a given objective aperture size.

In addition to hydrogen, Xe and Ar have been used in the microprobe. With Ar total and probe currents similar to hydrogen were observed. Current-voltage characteristics for Ar are shown in Fig. 22 where the pressure was estimated at  $2 \times 10^{-3}$  torr and a probe current of  $2 \times 10^{-11}$  amperes was measured, corresponding to a

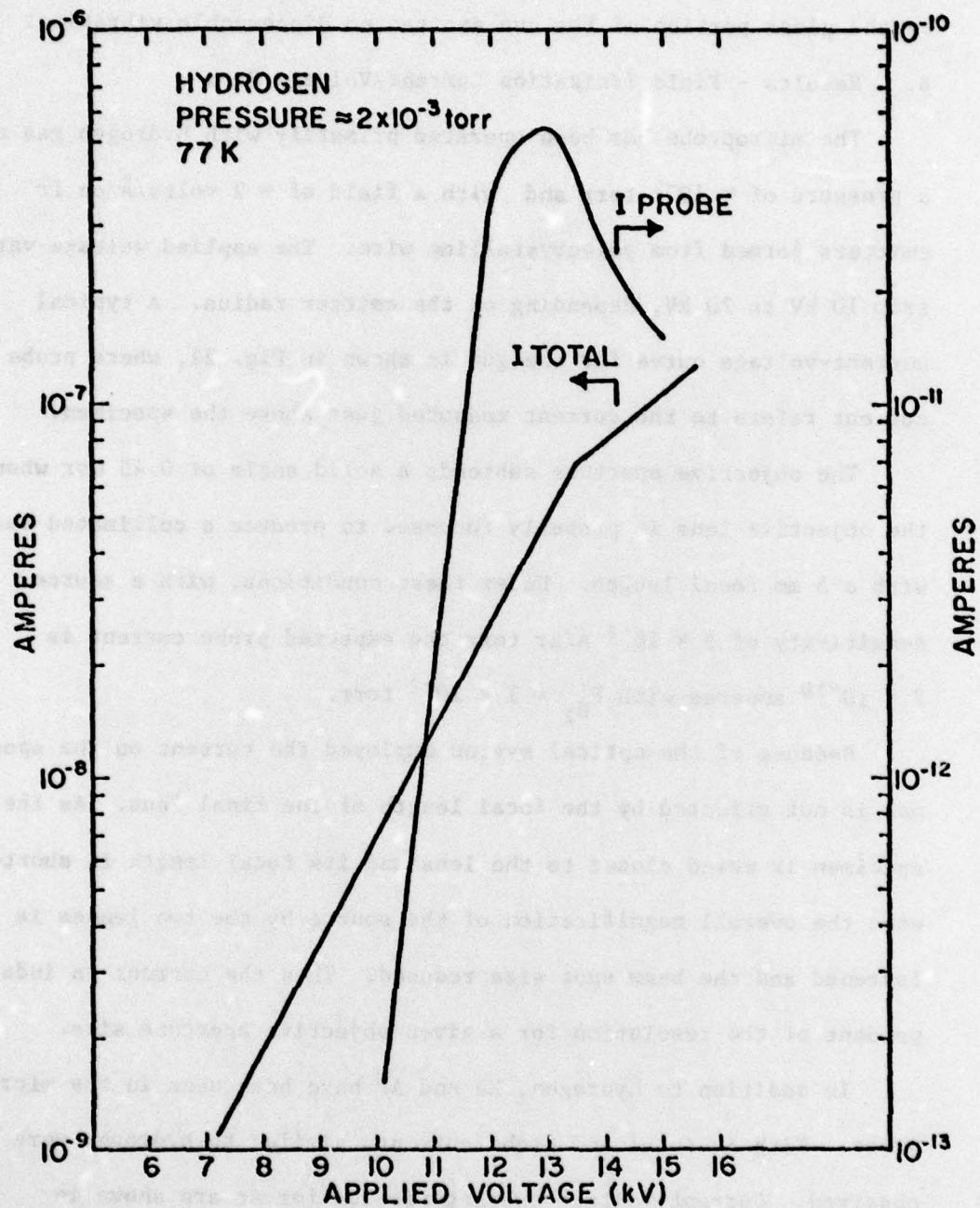


Fig. 21. Probe current and total current as a function of emitter voltage as measured in the SIM near the specimen. Angle subtended by the objective aperture was  $\alpha = 0.012$  rad.

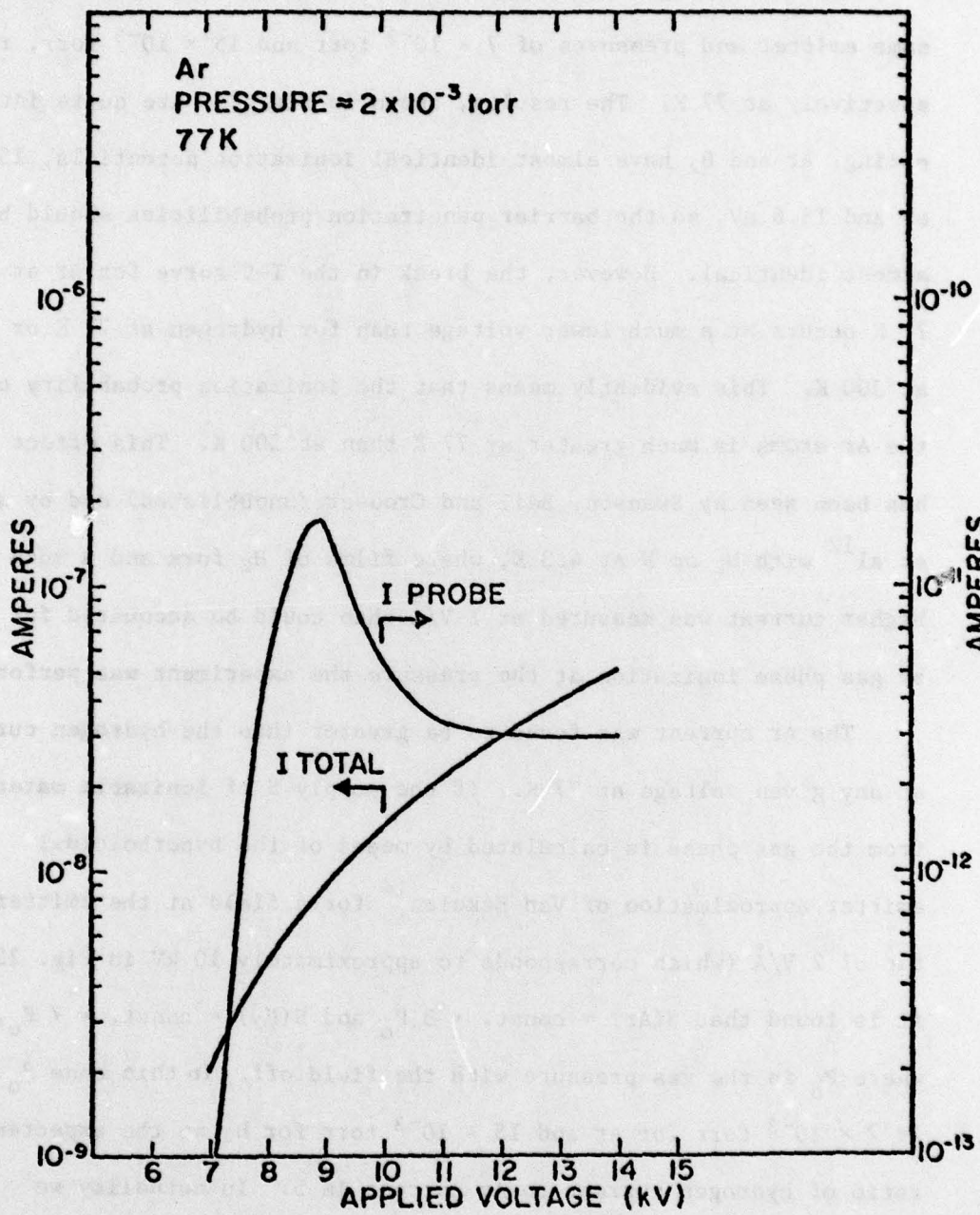


Fig. 22. Probe current and total current as a function of emitter voltage for Ar as measured in the SIM near the specimen,  $\alpha = 0.012$  rad.

sensitivity of  $6 \times 10^{-5}$  amperes/sr torr.

Current-voltage curves were taken for Ar and hydrogen with the same emitter and pressures of  $7 \times 10^{-3}$  torr and  $15 \times 10^{-3}$  torr, respectively at 77 K. The results, shown in Fig. 23, are quite interesting. Ar and H<sub>2</sub> have almost identical ionization potentials, 15.7 eV and 15.6 eV, so the barrier penetration probabilities should be almost identical. However, the break in the I-V curve for Ar at 77 K occurs at a much lower voltage than for hydrogen at 77 K or Ar at 300 K. This evidently means that the ionization probability of the Ar atoms is much greater at 77 K than at 300 K. This effect has been seen by Swanson, Bell and Crouser (unpublished) and by Jason et al<sup>12</sup> with H<sub>2</sub> on W at 4.3 K, where films of H<sub>2</sub> form and a much higher current was measured at  $1 \text{ V/\AA}$  than could be accounted for by gas phase ionization at the pressure the experiment was performed.

The Ar current was found to be greater than the hydrogen current at any given voltage at 77 K. If the supply S of ionizable material from the gas phase is calculated by means of the hyperboloidal emitter approximation of Van Eekelen<sup>14</sup> for a field at the emitter tip of  $2 \text{ V/\AA}$  (which corresponds to approximately 10 kV in Fig. 23), it is found that  $S(\text{Ar}) = \text{const.} \times 3 P_0$  and  $S(\text{H}_2) = \text{const.} \times 7 P_0$ , where  $P_0$  is the gas pressure with the field off. In this case  $P_0$  is  $7 \times 10^{-3}$  torr for Ar and  $15 \times 10^{-3}$  torr for H<sub>2</sub> so the expected ratio of hydrogen current to Ar current is 5. In actuality we see there was 5 times more Ar current than hydrogen current.

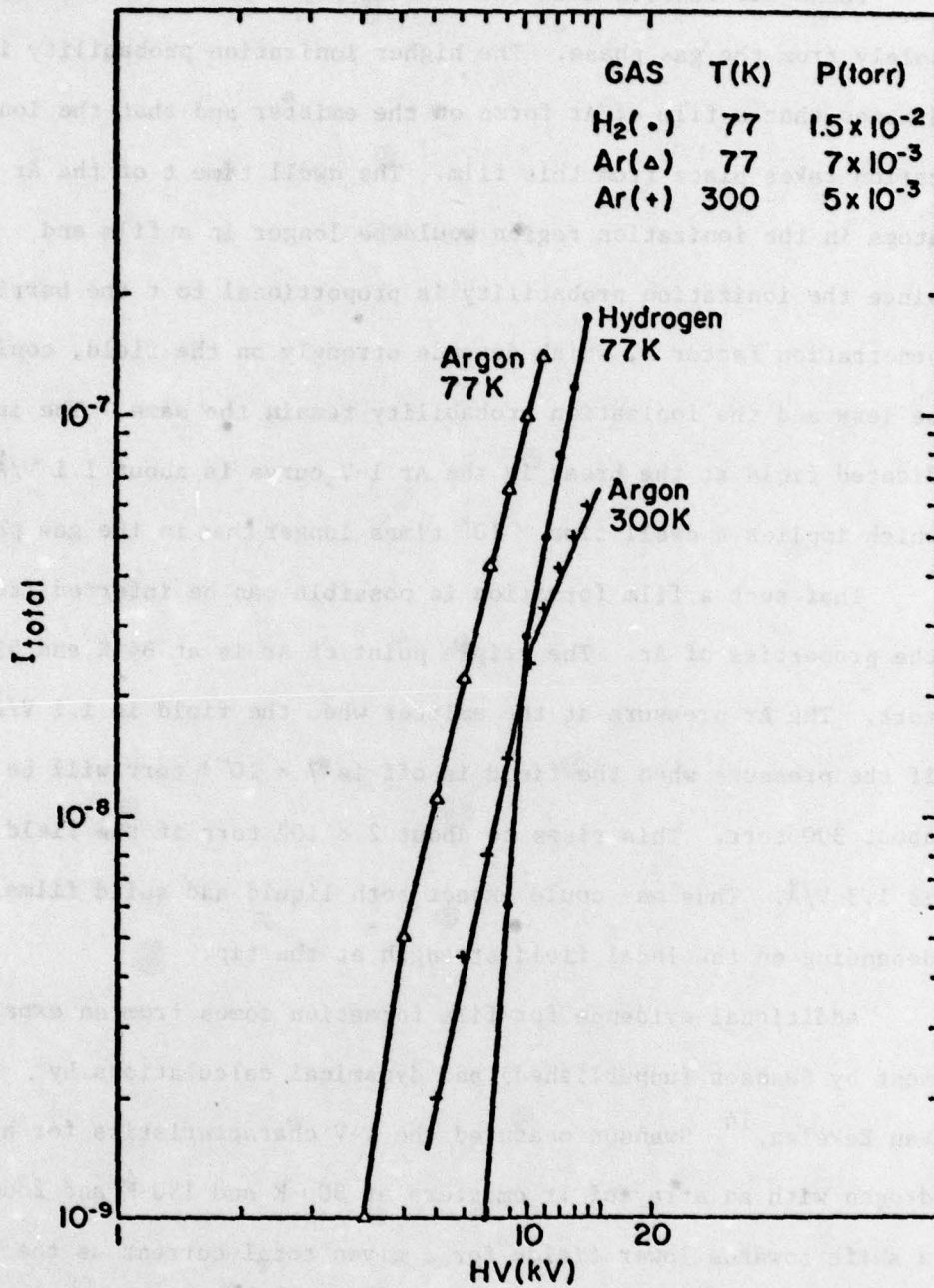


Fig. 23. Total current vs. voltage with the same emitter for H<sub>2</sub> and Ar gases. Note the shift in the I-V curve for Ar at 77 K. Ionization potentials are  $I_p = 15.7$  eV and 15.6 eV for Ar and H<sub>2</sub>, respectively.

These two results mean that the supply of Ar is not coming solely from the gas phase. The higher ionization probability indicates that a film of Ar forms on the emitter and that the ionization takes place from this film. The dwell time  $t$  of the Ar atoms in the ionization region would be longer in a film and since the ionization probability is proportional to  $t$  the barrier penetration factor  $D$ , which depends strongly on the field, could be less and the ionization probability remain the same. The indicated field at the break in the Ar I-V curve is about  $1.1 \text{ V/\AA}$  which implies a dwell time  $\sim 10^8$  times longer than in the gas phase.

That such a film formation is possible can be inferred from the properties of Ar. The triple point of Ar is at 84 K and 518 torr. The Ar pressure at the emitter when the field is  $1.1 \text{ V/\AA}$  if the pressure when the field is off is  $7 \times 10^{-3}$  torr will be about 300 torr. This rises to about  $2 \times 10^4$  torr if the field is  $1.3 \text{ V/\AA}$ . Thus one could expect both liquid and solid films, depending on the local field strength at the tip.

Additional evidence for film formation comes from an experiment by Swanson (unpublished) and dynamical calculations by Van Eekelen.<sup>14</sup> Swanson measured the I-V characteristics for hydrogen with an array of Ir emitters at 300 K and 150 K and found a shift towards lower fields for a given total current as the temperature was lowered, but the curves cross at higher fields. It is certain that hydrogen does not form films at these

temperatures. The same effect is predicted by Van Eekelen for He field ionized from the gas phase, i.e. a shift towards lower fields for given current and a convergence of the characteristic curves at high fields. In the case of Ar, the curves diverge at higher fields, indicating the supply mechanism is not pure gas phase. Different results were found with Xe. The total currents were similar to hydrogen again but now the probe current was very low, as shown in Fig. 24. The ratio of Xe to hydrogen current at 77 K and  $3.5 \times 10^{-3}$  torr with a field of  $2 \text{ V/\AA}$  is unity, based on gas phase supply considerations. This is what was measured. Since the triple point of Xe is at 161 K and 616 torr, and the pressure at the emitter tip at  $2 \text{ V/\AA}$  is 10 torr, a solid layer will form. Evidently the Xe does not diffuse up the emitter shank to the ionization zone, since the current is what one would expect from pure gas phase supply.

With methane ( $\text{CH}_4$ ) the probe current at 77 K was also small (see Fig. 25). The triple point of  $\text{CH}_4$  is at 90.6 K and a pressure of the order of 0.6 atmosphere ( $\approx 500$  torr). With a polarizability of  $2.6 \text{ \AA}$  the conditions at the emitter tip are at lower temperature and much higher pressure than the triple point, leading to the formation of solid methane. Evidently, as in the case of Xe at 77 K the diffusion of  $\text{CH}_4$  is small enough that most ionization takes place down the shank.

### C. Noise Measurements

Previous measurements<sup>15</sup> of the signal to noise ratio (S/N) on the FI source at room temperature in a high vacuum system showed that

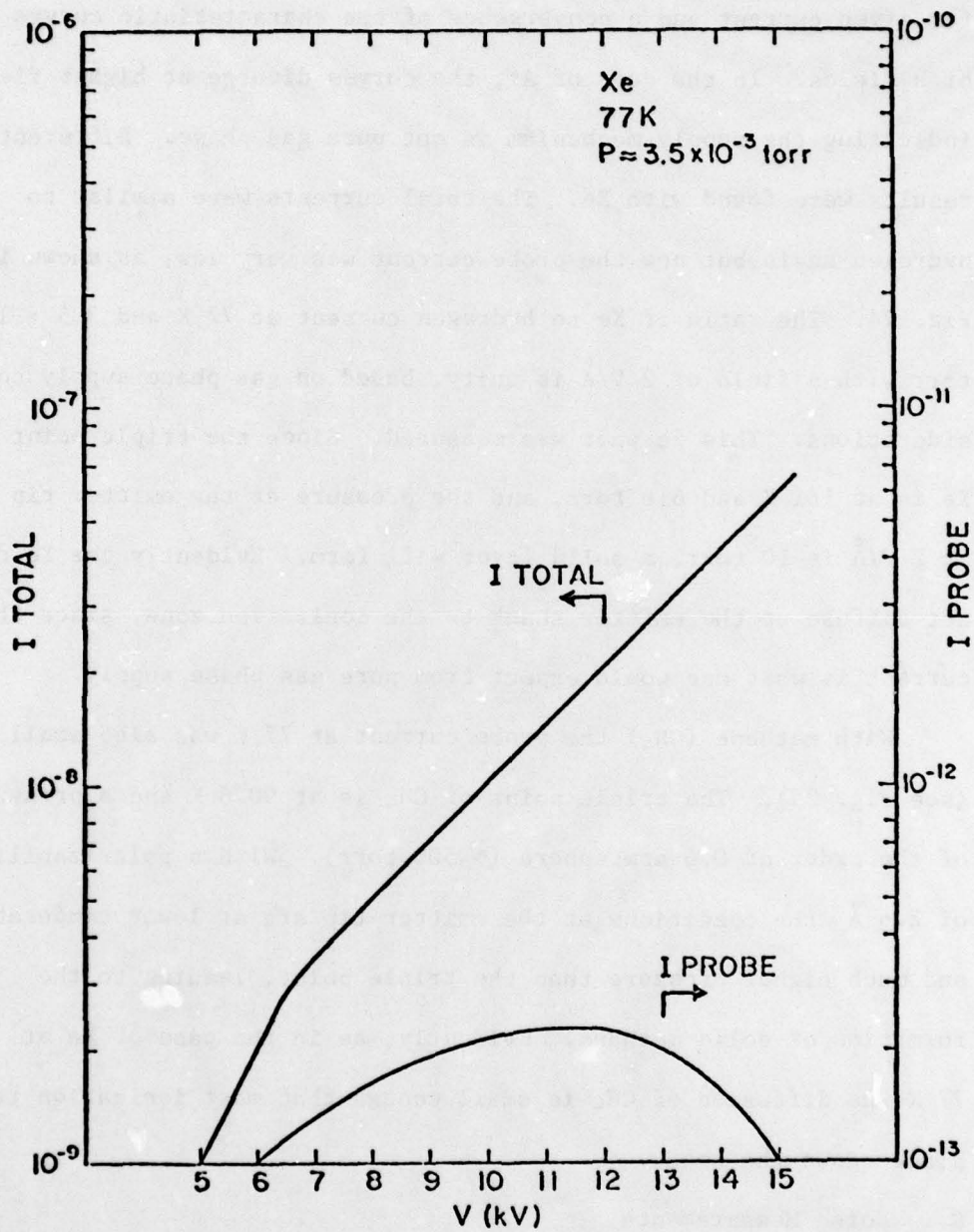


Fig. 24. Total current and probe current as a function of emitter voltage for Xe at 77 K.

S/N improved as the current was increased and that the noise power spectrum fell almost entirely between 0 and 30 Hz. Measurements made on the current on target in the SIM with the FI source at 77 K show the same behavior. In the first case the current was increased twofold by increasing the source gas pressure and S/N improved twofold as well. In the latter case the current was increased approximately threefold by increasing the voltage applied to the emitter and S/N improved by the same ratio.

In the SIM the objective aperture subtended 0.15 msr, the maximum detected current on the specimen was  $7 \times 10^{-11}$  amperes and S/N = 43 in the interval 1 - 11 Hz, as measured with a spectrum analyzer. The noise spectrum was also analyzed by recording it on a wideband tape recorder and analyzing it with a computer program which performs a Fourier composition of the signal with  $\Delta f = 2$  Hz. The result of this analysis is shown in Fig. 25. On the same scale the shot noise current for  $\Delta f = 10$  Hz would be at approximately 0.06, with  $\langle I_{\text{SHOT}}^2 \rangle = 2eI\Delta f$ .

In the previous work<sup>15</sup> it was found that the angular distribution of hydrogen extended out to  $\approx 18^\circ$ . When the emitter was placed so the source aperture subtended  $\approx 27^\circ$ , S/N was  $\approx$  twice what was measured when the emitter was moved away from the aperture to the point where the aperture subtended  $\approx 14^\circ$ . The most likely explanation for this effect is that ions striking the aperture with energy  $E_0$  cause adsorbed gas molecules to be liberated. The molecules which are negatively ionized in this process will be accelerated back to the

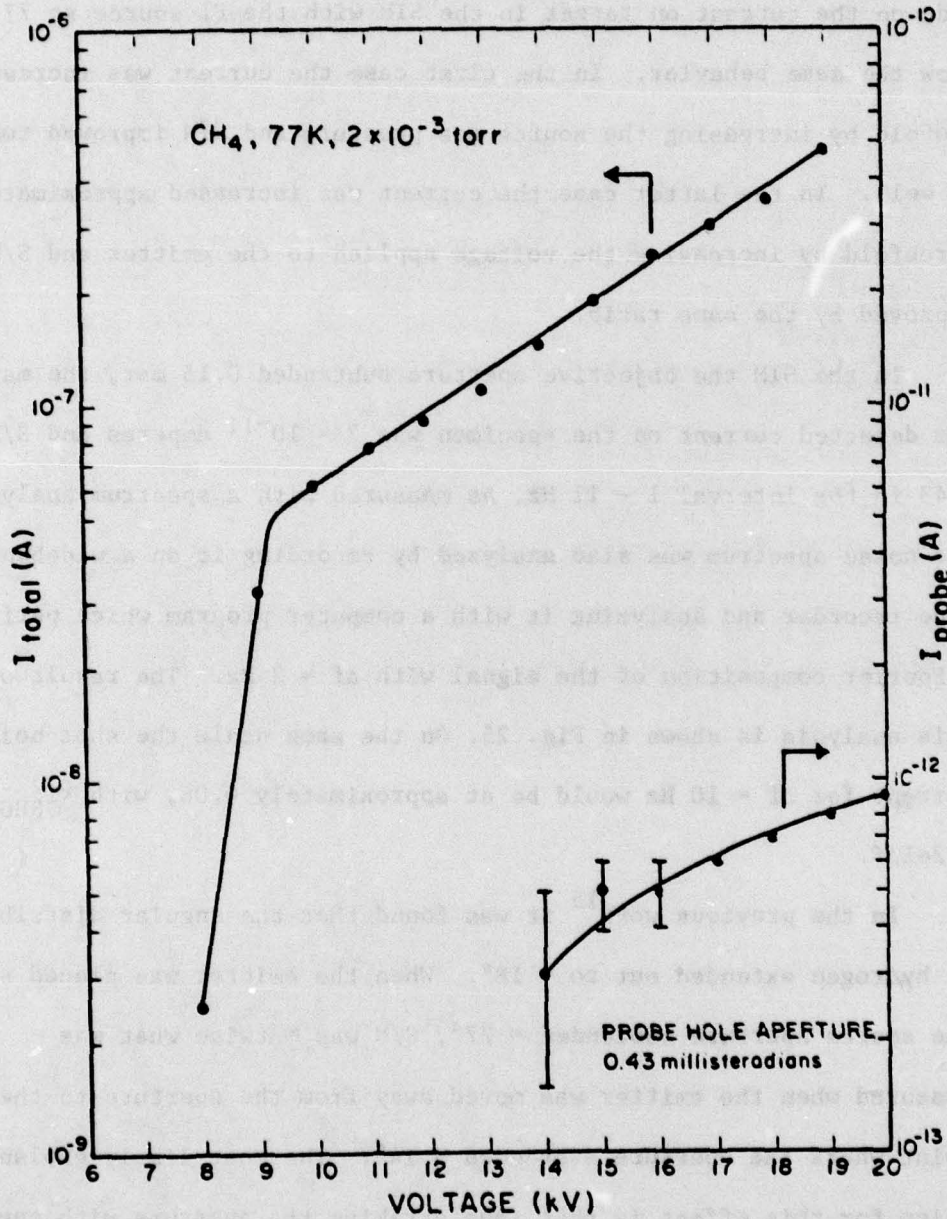


Figure 25. Total and probe current as a function of emitter voltage for methane at 77 K and a pressure of  $2 \times 10^{-3}$  torr.

emitter where they will cause sputtering damage. This can be expected to affect current generation at the emitter tip.

When the current from the FI source is allowed to fall directly on a phosphor screen as in a FI microscope, various sites on the emitter tip from which current originates can be seen with the eye to turn on and off. Presumably it is this phenomenon which is responsible for the low frequency noise and it is most likely caused by local changes in gas supply due to changes in emitter geometry or coverage by adsorbed gases.

As mentioned above, the field emitters used here have not been field evaporated, but they are flashed briefly before use. The exact state of the emitter surface is not known so that it is difficult to specify mechanisms for noise generation. It is known that surface adsorbates affect ionization rates, and so changes in amounts and location of adsorbates could be important. At the fields used to ionize hydrogen,  $\approx 2 \times 10^{10}$  volts/meter, there are numerous gases which can reach the emitter or emitter shank without being ionized.

## REFERENCES

1. E. W. Müller and T. T. Tsong, *Field Ion Microscopy*, American Elsevier Publishing Co., p. 120 (1969).
2. Supplied by J. D. Verhoeven, Iowa State University, Ames, Iowa 50010.
3. K. Bober and Z. Mirea, *Surface Science* 51, 513 (1975) and J. L. Wang and R. Vanselow, *Surface Science* 43, 21 (1974).
4. L. W. Swanson, *J. Vac. Sci. Technology* 12, 1228 (1975).
5. P. C. Bettler and F. M. Charbonnier, *Physical Review* 119, 85 (1960).
6. J. P. Barbour et al., *Phys. Rev.* 117, 1452 (1960).
7. P. C. Bettler and G. Barnes, *Surface Science* 10, 165 (1958).
8. A. J. Melmed, *J. Appl. Phys.* 38, 1885 (1967).
9. J. Orloff and L. W. Swanson, *Annual Report, Murdock Foundation, Beaverton, Oregon* (1977).
10. J. W. Gadzuk and E. W. Plummer 3, 2125 (1971).
11. E. L. Murphy and R. H. Good, *Phys. Rev.* 102, 1464 (1956).
12. L. W. Swanson, *J. Vac. Sci. Technol.*, 12, 1228 (1975).
13. A. Jason et al., *J. Chem. Phys.* 52, 2227 (1970).
14. H. A. M. Van Eeklen, *Surface Science* 21, 21 (1970).
15. J. O. Orloff and L. W. Swanson, *J. Vac. Sci. Technol.*, 12, 1209 (1975).